High-temperature fracture behavior of an α/β Titanium alloy manufactured using laser powder bed fusion

Meishen Xie [a b], Sheng Huang [b], Zhi Wang [a], Upadrasta Ramamurty [b c]

[a]

National Engineering Research Center of Near-net-shape Forming for Metallic Materials, South China University of Technology, Guangzhou 510641, PR China

[b]

School of Mechanical and Aerospace Engineering, Nanyang Technological University, Singapore 639798, Republic of Singapore

[c]

Institute of Materials Research Engineering, Agency for Science, Technology and Research, Singapore 138634, Republic of Singapore

Abstract

The room and high temperature (up to 600 °C) mechanical properties, with emphasis on the fracture toughness and fatigue resistance, of an α/β titanium alloy that was additively manufactured using the laser powder bed fusion (LPBF) technique were evaluated in the as-printed (α' lath martensite with negligible β phase content) and heat-treated (α/β structure with a significant volume fraction of the β phase) states for critically examining the β phase's role in the fracture and fatigue behavior (given the significantly higher diffusion rates of various species in β compared to α). Experimental results reveal that the heat-treated sample exhibits superior ductility and fracture initiation toughness at elevated temperatures, compared to the as-printed sample, due to the presence of β ligaments in the former. They also prevent strain localization along the prior β grain boundaries, and their absence in the as-printed state leads to cracking along those boundaries. While the fatigue crack growth (FCG) rates in both the as-printed and heat-treated samples deteriorated with increasing temperature, the threshold for FCG generally increased, which is attributed to creep-induced crack tip blunting. Moreover, a double Paris exponent phenomenon is observed for the heat-treated sample at 300 °C, attributed to the hydrogen-assisted crack growth, with β phase providing an accelerated diffusion pathway. Overall, the experimental results and their analyses illustrate the intricate relationship between creep, hydrogen diffusion, and the β phase in dictating the fracture behavior of LPBF α/β titanium at elevated temperatures.

Graphical abstract

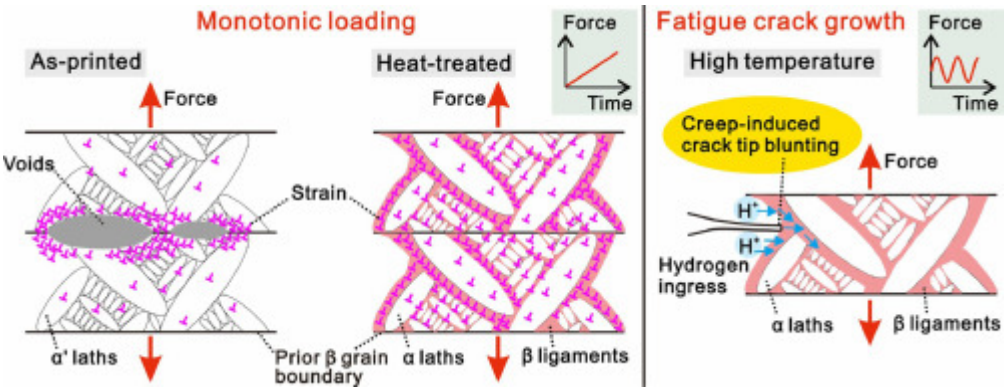

Keywords

Laser powder bed fusion

Titanium alloy
High temperature
Fatigue crack growth
Fracture toughness

1. Introduction

Additive manufacturing (AM) of a wide range of α- to β-based Ti alloy structural components, using techniques such as laser Powder Bed Fusion (LPBF), has been extensively explored for aerospace and biomedical industrial applications, where considerations such as weight reduction and bespoke design are important [[1], [2], [3], [4], [5], [6], [7], [8], [9], [10], [11], [12], [13]]. While Ti-6Al-4V (α/β Ti) is the most widely studied LPBF Ti alloy [[14], [15], [16]], the insights gained are not limited to it alone, but can be extended to a broader spectrum of the α/β variants and are even applied to near-α alloys. The high cooling rates and directional solidification, inherent to the LPBF process, result in the formation of α' martensite within the columnar prior β grains, accompanied by prevalent lattice defects [[17], [18], [19]]. This microstructure often offers higher strength at the cost of ductility vis-à-vis conventionally manufactured (CM) and mill-annealed Ti-6Al-4V. The reported mode I fracture toughness, K_{IC}, values in the as-printed (AP) state are also typically lower (in the range of 16 – 67 MPa$\sqrt{m}$ [2,20,21]), in comparison to those of wrought Ti-6Al-4V (30 – 100 MPa$\sqrt{m}$) [22]. Some studies attribute the reduced ductility of LPBF Ti-6Al-4V to the partial decomposition of α' microstructure containing a limited amount of isolated thin β lamellae [7,23,24]. These observations find support in the *in-situ* X-ray diffraction results of Zhang et al. [25], where the nano-scale β phase exhibited much greater lattice strain than the α/α' matrix, while the lattice strain difference between the fully transformed α and β phases was significantly reduced. Kumar and Ramamurty demonstrated that through a duplex heat treatment performed at sub-β transus temperatures, a K_{IC} of ~100 MPa$\sqrt{m}$ for LPBF Ti-6Al-4V could be achieved [3].

Ti alloys also exhibit both high specific strength and corrosion resistance at intermediate temperatures, up to 600 °C, depending on their α/β stability. For instance, the α/β Ti alloys like Ti-62222, Ti-5524S, or Ti-17 can be utilized up to ~400 °C [26]. In contrast, the near-α Ti alloys (also containing α and β, but β-stabilized to a lesser degree), such as TA15, Ti-6242S, IMI 834 and Ti-1100, can operate up to 600 °C [8,[27], [28], [29]]. Performance of these alloys have also been proven in the context of LPBF; Zhu et al., for example, demonstrated that heat-treated Ti-6242S possesses high room and elevated temperature (500 °C) yield strengths (YS) of 992 and 706 MPa, respectively [6]. Fleißner-Rieger et al. found that heat-treated LPBF Ti-6242S exhibited substantially improved strength at 250 and 500 °C, compared to its cast and annealed counterpart [30]. Furthermore, TiC/graphene-reinforced Ti-6Al-4V composites was found to exhibit higher yield strengths than those of the Ti-6Al-4V alloy up to 600 °C [31]. Zhang et al. reported that after heat treatment, the activation of pyramidal <*c* + *a*> slip systems at 500 °C in LPBF TA15 effectively reduced strain localization and the propensity for cracking during mechanical loading [13]. Beyond 600 °C, the mechanisms of (i) substantial brittle oxide scale formation, which can also rupture on its own [32,33], and (ii) excessive interstitial oxygen ingress/diffusion, which leads to embrittlement with less than 1 at.% oxygen concentration [[33], [34], [35]], result in the deterioration of the mechanical properties of Ti alloys, limiting their applicability.

During the plastic deformation of the α/β Ti alloys, strain primarily accumulates in the β ligaments, as demonstrated in studies on Ti-6242S [6], TA15 [8], and TiB-reinforced Ti-6Al-4V [36]. In instances where the volume fraction of the prior β ligament is negligible, cracking along the prior β boundary has

been observed in LPBF TA15 that was tensile tested at 500 °C [8]. Such cracking is also influenced by the test temperature. Fractography on the Ti-6Al-4V samples tensile tested at 350 and 450 °C indicates ductile fracture characteristics (Ultimate Tensile Strength (UTS) ~ 832 – 927 MPa), while at 550 °C (UTS ~ 535 – 573 MPa), the surfaces exhibit intergranular fractures along the prior β boundaries [37]. The addition of 2 vol% TiB to Ti-6Al-4V effectively eliminates the prior β boundary cracks after creep rupture [36]. This elimination is attributed to the load transfer effect facilitated by the widely distributed TiB whisker clusters, where strain accumulation can be delocalized [38].

Other high-temperature degradation modes were also studied for LPBF Ti alloys. Unnotched fatigue tests performed at 400 °C showed that LPBF Ti-6Al-4V exhibits higher cyclic softening compared to that at room temperature, leading to faster crack growth [39]. Residual stress significantly influences the unnotched fatigue properties at 300 °C [40]. Moreover, manufacturing defects continue to adversely affect these properties up to 650 °C [40,41]. Spigarelli et al. performed creep tests on LPBF Ti-6Al-4V at 500 – 650 °C, showing that the creep was climb controlled [42].

Prior studies on the high-temperature mechanical responses of LPBF Ti alloys have predominantly focused on examining the tensile properties using unnotched specimens. A comprehensive understanding of the structure-property correlations, particularly concerning the unique LPBF microstructure's influence on the damage tolerance attributes such as fracture toughness and fatigue crack growth (FCG) resistance at elevated temperatures, is yet to be developed. This is surprising, especially given the well-established use of conventionally manufactured counterparts of these alloys in high-temperature applications. With this in mind, a detailed investigation of the mechanical performance of a LPBF α/β alloy was performed, considering both (a) temperature and (b) microstructure before and after heat treatment. We evaluated uniaxial tensile properties, mode I fracture toughness, and FCG characteristics of these materials at room temperature, 300, 500, and 600 °C in two distinct alloy states: as-printed (featuring α' martensitic laths) and post-dissolution heat treatment (aimed at precipitating β ligaments while retaining the primary lath size). The β phase, known for its higher diffusivity compared to the α phase, can lead to significant differences in behavior at elevated temperatures where diffusion becomes a critical factor [43]. Hence, this investigation presents a detailed exploration of a LPBF α/β alloy (Ti-6Al-3Mo-1Zr (wt.%))'s mechanical behavior at high temperatures. Note that this alloy's composition varies with that of widely explored α/β Ti alloy: Ti-6Al-4V. The use of Mo in place of V is expected to improve the high-temperature properties, due to its relatively larger atomic size and slower diffusivity. However, the overall nature of fracture behavior and microstructural evolution with temperature are expected to be generally applicable to all α/β Ti alloys.

2. Materials and experiments

2.1. Materials

The Ti-6Al-3Mo-1Zr (wt.%) alloy blocks examined in this study were fabricated on a Ti-6Al-4V substrate using a commercially available LPBF machine (EOSINT 280), equipped with a Yb:YAG fiber laser with the following specifications: (1) wavelength: 1060 - 1100 nm, (2) spot diameter: 80 μm, (3) maximum power: 400 W, and (4) Gaussian power distribution. The process took place in an argon environment (with the oxygen content controlled to below 1000 ppm to limit sample contamination). The pre-alloyed powder employed for sample fabrication was produced through the electrode induction-melting inert gas atomization (EIGA) process, resulting in a spherical morphology as illustrated in Figure S1 of the Supplementary Information (SI). The powder has a size distribution ranging from 15 to 53 μm, with a median size (D_{50}) of ~32 μm.

The fabrication process involved a stripe scanning strategy (stripe width of 5 mm and stripe overlap of 120 μm), schematically illustrated in Fig. 1a, along with a 67° clockwise rotation after the completion of each layer. Prior optimization of the LPBF process parameters resulted in the utilization of the following settings: (1) laser power, *P*: 170 W, (2) scanning speed, *v*: 1050 mm/s, (3) layer thickness, *t*: 30 μm, and (4) hatch spacing, *d*: 100 μm. These process parameters translated to a volumetric energy density, $E_d = P/(v \times d \times t)$, of ~54.0 J/mm^3.

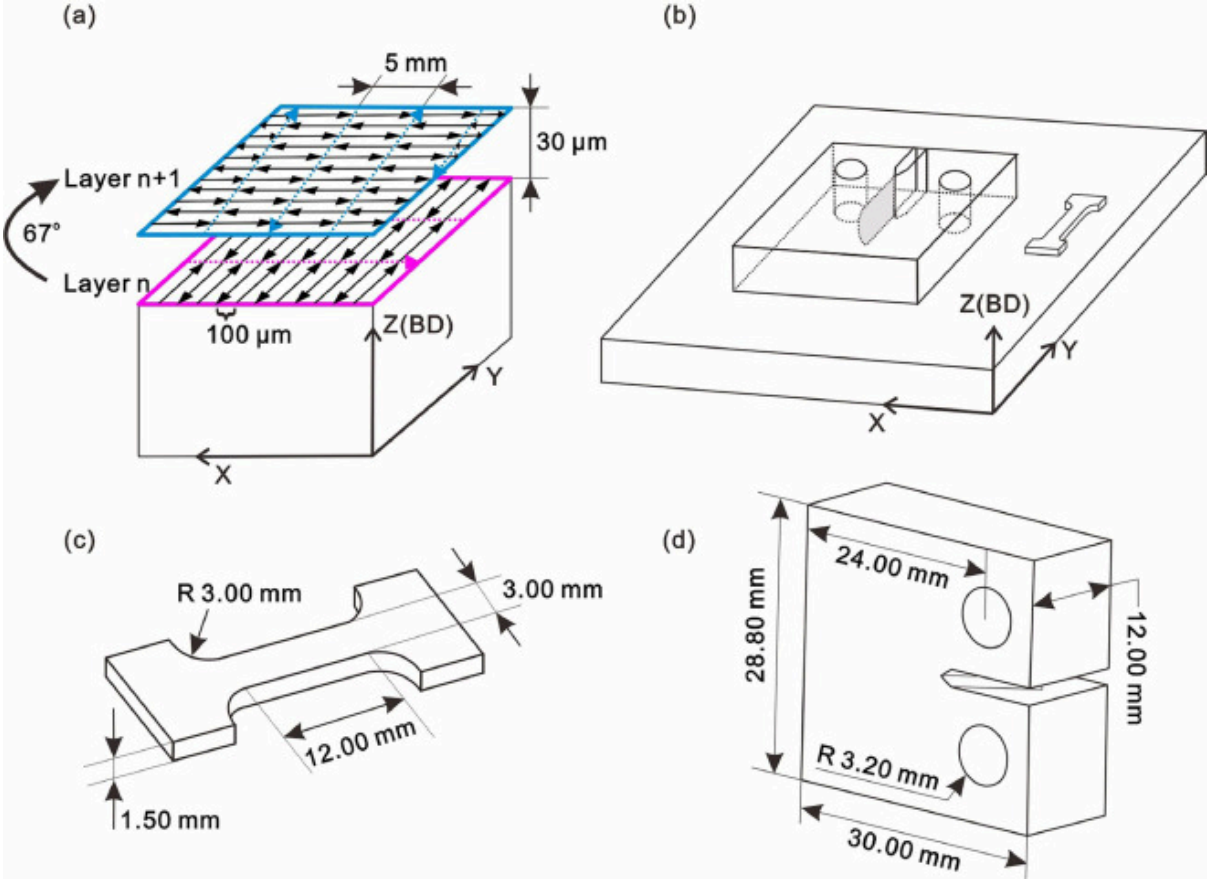

1. Download: Download high-res image (522KB)
2. Download: Download full-size image

Fig. 1. Schematics of (a) stripe scanning strategy, (b) relative orientation of tensile and C(T) specimens to the substrate, and the dimensions of (c) tensile and (d) C(T) specimens.

Two types of blocks were manufactured and wire-cut to achieve the required final dimensions. The first set are 30 mm in length, 7 mm in width, and 6 mm in height and were machined into tensile coupons for the purpose of conducting tensile tests. The second set are 32 mm in length, 32 mm in width, and 15 mm in height. These blocks were machined into compact tension C(T) specimens (thickness (B) 12 mm and width (W) 24 mm), for evaluating the material's FCG and fracture toughness properties. The schematic orientation of these specimens in relation to the substrate is illustrated in Fig. 1b, while the dimensions of the tensile and C(T) specimens are provided in Figs. 1c and d, respectively. Additionally, a subset of these specimens was vacuum heat treated at 800 °C for 2 h, followed by furnace cooling, so as to transform the microstructure consisting of the acicular α' phase in the as-printed state to a lath α + inter-lath β phase microstructure, such that the effect of β phase on the overall fracture behavior can be probed. Hereafter, the as-printed and heat-treated samples will be referred to as AP and HT, respectively, followed by the temperature at which they were tested.

For example, AP-RT and HT-500 refer to the as-printed sample tested at room temperature and heat-treated sample tested at 500 °C, respectively. Subsequent micrographical analysis confirmed that the AP and HT samples have a relative density exceeding 99.9 %. Representative micrographs are shown in Figure S2, illustrating the types of defects found in the specimens, mainly lack-of-fusion defects and gas pores, with negligible presence of keyhole pores. The minimal porosity content has negligible effects on the fracture behavior as the study does not include unnotched fatigue tests.

Inductively Coupled Plasma Optical Emission Spectroscopy analysis, as well as Inert Gas Fusion experiments were performed for evaluating the oxygen and hydrogen contents in the AP and HT samples, for identifying the differences in chemical compositions, if any, after heat treatment, which were found to be negligible, as shown in Table 1.

Table 1. Chemical composition of the Ti-6Al-3Mo-1Zr alloys (wt.%) in AP and HT states.

Sample	Al	Mo	Zr	O	H	Ti
AP	5.88	3.06	0.96	0.16	0.0045	Bal.
HT	5.86	3.05	0.95	0.16	0.0044	Bal.

2.2. Experiments

The surfaces intended for microstructural analysis were mirror-polished using successively finer SiC papers, followed by 3 µm diamond and 0.04 µm SiO_2 + H_2O_2 suspensions. Subsequent observations were conducted on these surfaces using optical microscopy (OM) and scanning electron microscopy (SEM). Additionally, electron backscatter diffraction (EBSD) scanning was performed to investigate the microstructural characteristics. This process utilized an Aztec HKL Oxford detector integrated with SEM, employing a maximum step size of 0.5 µm. X-ray diffraction (XRD) was performed on the prepared surface using the Cu-Kα radiation (λ = 1.54056 Å). Some samples were further processed using a twin-jet electropolisher for transmission electron microscopy (TEM) studies for characterizing the nanoscale features, with imaging modes including high-resolution TEM (HR-TEM), selected area electron diffraction (SAED), High-angle annular dark-field scanning transmission electron microscopy (HAADF-STEM), and STEM-energy-dispersive X-ray spectrometry (EDX).

Uniaxial tensile, fracture toughness, and FCG tests were conducted at room temperature (RT, ~25 °C), 300, 500, and 600 °C. Tensile tests were performed with a crosshead velocity of 0.72 mm/min on a universal testing machine (UTM) equipped with a furnace and video extensometer, following the ASTM standard E8/E8M-22 [44]. The samples were held for 15 min at the intended test temperature before testing, and a minimum of three tensile samples were examined for each condition. The K_{IC} and FCG measurements were performed on at least two C(T) specimens. Prior to K_{IC} measurements, the samples were subjected to fatigue pre-cracking in accordance with the ASTM standards E399–23 [45] and E647–23a [46]. This involved using a servo-hydraulic UTM to achieve an a/W ratio of approximately 0.45 – 0.55, where a is the crack length and W is the width of the specimen. A tensile load with a sinusoidal waveform at a frequency of 10 Hz and a load ratio (R) of 0.1 was applied to the samples. Both the surfaces of the C(T) specimens were mirror polished prior to testing, which enabled the monitoring of crack growth through a camera, affixed to a long-distance optical microscope, capable of 60X magnification. Following the pre-cracking process, the specimens were quasi-statically pulled until fracture at a displacement rate of 0.002 mm/s. A soaking time of 1.5 h was utilized before conducting K_{IC} and FCG measurements for each specific temperature condition. A significantly longer soaking time (compared to that used in the tensile tests) was employed for the following two reasons: 1) The C(T) specimens are thicker, 2) To ensure that the FCG tests, which are prolonged in

nature, are minimally affected by any in-operando phase transformations, such that the data points within a particular test condition are cross-comparable, and 3) in cognizance of the fact that FCG in actual service situations happens over a prolonged service time.

The load shedding method, in accordance with the ASTM E647–23a standard [46], was employed to determine the threshold stress intensity factor range for fatigue crack initiation (ΔK_o). For ΔK_o measurements, the applied stress intensity factor range (ΔK) was incrementally reduced by ~5 % after every 0.2 mm of crack growth until the crack growth rate per cycle, da/dN, is below ~2 × 10^{-10} m/cycle. The specific ΔK value at which this criterion was met was designated as ΔK_o. In this procedure, the data obtained from da/dN vs. ΔK during the steady-state crack growth regime were fitted with the Paris equation: $da/dN = C(\Delta K)^m$, where C and m represent material properties and are respectively referred to as the Paris constant and Paris exponent.

Postmortem analyses were carried out on the fractured tensile, fatigue pre-cracked C(T), and mode-I fractured C(T) samples using SEM and TEM. In cases where necessary, the side surfaces of the samples were carefully polished to eliminate the oxide layer for enhancing the backscatter electron (BE) image contrast in SEM.

3. Results

3.1. Phase constituent and micro-structure

XRD patterns obtained on the AP and HT Ti-6Al-3Mo-1Zr alloy are shown in Figs. 2a and b, respectively. The XRD patterns following exposure at 300, 500, and 600 °C for over 60 h are also presented. The elevated temperature exposures were carried out after the completion of the FCG tests, specifically in areas considerably away from the maximum plastic zone size. The duration of this exposure is indicated as a range due to the variable durations of the elevated temperature FCG tests.

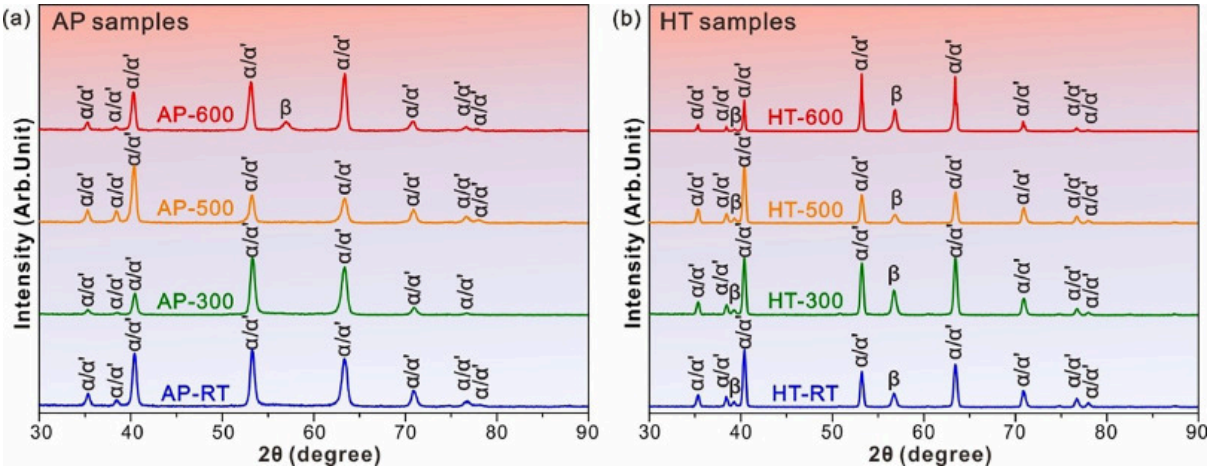

1. Download: Download high-res image (678KB)
2. Download: Download full-size image

Fig. 2. Postmortem XRD analysis of (a) AP and (b) HT in the stress-free region (only exposed to the corresponding test temperature).

The absence of a β phase peak in the XRD suggests a predominant α' phase in AP-RT. Analogous to the response observed in Ti-6Al-4V, heat treatment above 400 °C results in the decomposition of α' phase into α+β [47], as evidenced by the appearance of β peaks after AP's exposure to 600 °C and in the HT condition. Partial decomposition of the α' phase in the AP sample after exposure at 500 °C is insufficient to result in the β phase detection by XRD. (However, this phenomenon can be observed via TEM; results presented in a later section.) It is noteworthy that this alloy shares the same Al

concentration and similar β stabilizer content as Ti-6Al-4V (where the Molybdenum equivalent for the 4 wt.% Vanadium content is calculated to be 2.7 wt.% [4,48]).

In Fig. 3, the representative microstructures and textures of the lath α/α' phases and the prior β grains in both the AP and HT samples are displayed. Additionally, Fig. 4 provides higher magnification views of the same, revealing changes due to the thermal processing. A summary of the microstructural characteristics and length scales is provided in Table 2. The AP sample's microstructure, illustrated in Figs. 3a-c and Figs. 4a and b, showcases typical α' acicular lath martensite, commonly observed in the α/β titanium alloys such as Ti-6Al-4V [2,47,49]. The volume fraction of the inter-lath β, estimated using the SEM images that are obtained under BE mode, is approximately 21.3 %. For reference, when heat-treated at temperatures below the β-transus temperature, it was reported that LPBF Ti-6Al-4V contains ~14 to 22.5 % inter-lath β phase [3]. Upon heat treatment, discernible changes in microstructure become evident, characterized by the α' phase's decomposition into lamellar α + β ligaments, as shown in Figs. 4c and d. This supports the inferences made from the XRD results. The heat treatment is specifically employed such that the general morphology of the microstructure remains, but with the decomposition of α'. This way, the microstructure of α/β titanium alloys unique to LPBF can be probed, which is without the β phase, and be compared to one that has the β phase at the inter-lath region.

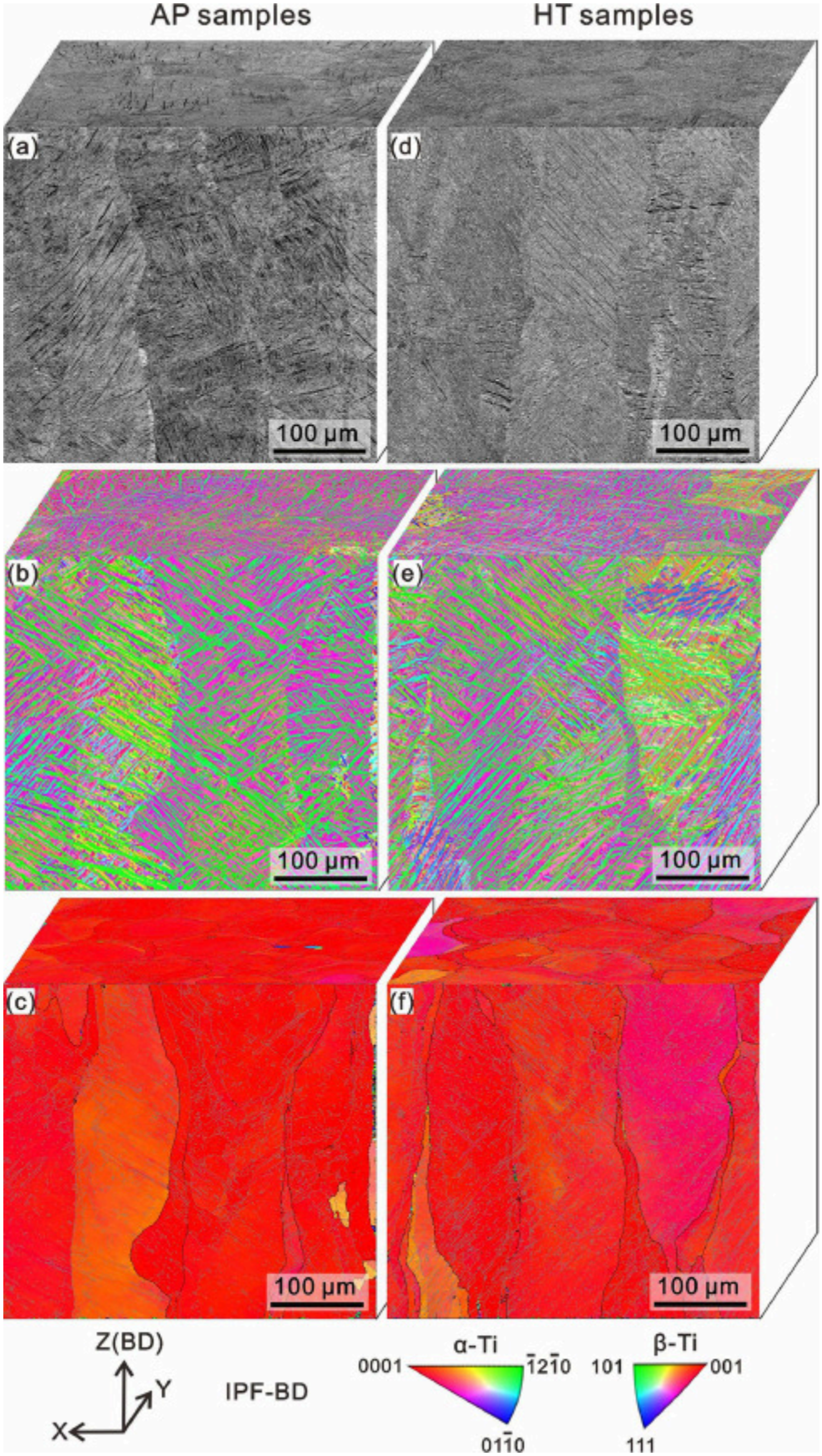

1. Download: Download high-res image (4MB)
2. Download: Download full-size image

Fig. 3. Representative microstructure and texture of (a-c) AP and (d-f) HT: (a, d) microstructure under BSE imaging mode, (b, e) grain orientation maps, and (c, f) reconstructed prior β grain orientation maps corresponding to (b) and (e). The inverse pole figure coloring in (b, c, e, f) corresponds to the build direction.

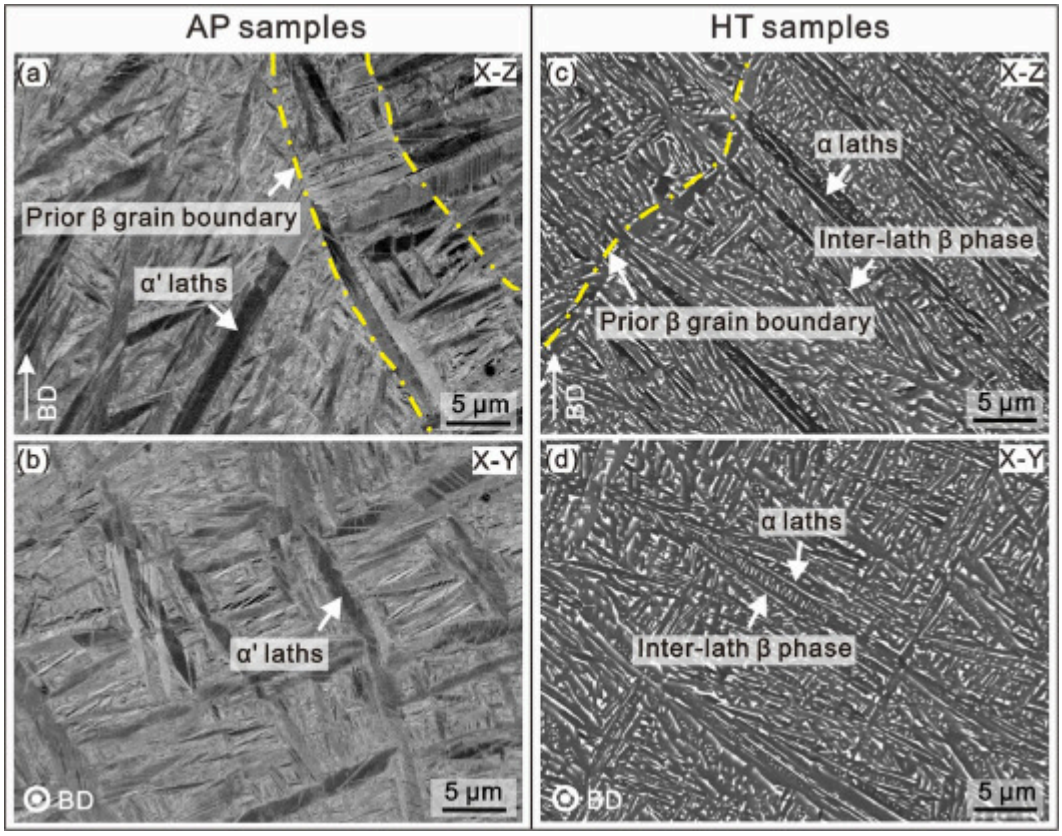

1. Download: Download high-res image (1MB)
2. Download: Download full-size image

Fig. 4. Representative microstructure for (a, b) AP and (c, d) HT at higher magnification.

Table 2. Summary of the microstructural statistics for AP and HT.

Sample	Constituent phase	Morphology	Volume fraction of β (vol.%)	Average prior β size, λ_β (μm)	Average lath size, λ_α (μm)
AP	α’	Acicular	N.A.	145.6 ± 19.7	1.7 ± 0.4
HT	α+β	Lamellar	21.3 ± 0.7	156.3 ± 30.9	1.8 ± 0.4

The grain orientation maps displayed in Fig. 3b and Fig. 3e show that the AP and HT samples have the Widmanstätten lath microstructure. After heat treatment, a marginal widening of the lath α/α’ structure can be observed, increasing from ~ 1.7 to ~ 1.8 μm. No recrystallization resulted from the heat treatment, and a similar observation is evident from the reconstructed prior β orientation map. Both the AP and HT samples predominantly exhibit a fiber β texture, wherein the 〈001〉 easy growth axis of the bcc phase aligns with the build direction (BD), as illustrated in Fig. 3c and Fig. 3f (with pole figure shown in Figure S3). This phenomenon, frequently encountered in LPBF, arises from the overall thermal gradient that runs anti-parallel to BD, and is associated with the epitaxial growth of grains in alloys with a low growth restriction factor [50]. The average width of the prior β grains in the AP and HT samples is comparable, ~ 145.6 and ~ 156.3 μm respectively. The fiber texture along BD corresponds to the presence of primary α/α’ laths oriented at around 45° to BD. This orientation relationship reflects

the allotropic transformation from bcc-β to hcp-α' via a diffusionless shear mechanism and dilatation, adhering to the Burgers orientation relationship of $\{0001\}_\alpha//\{110\}_\beta$. This transformation is driven by the rapid cooling rates of $10^3 - 10^5$ K·s^{-1} during the LPBF process [16,49,51,52]. Consequently, high-density of stacking faults, twins, and dislocations are observed in the α' phase, arising from the considerable residual stresses inherent to the AP LPBF components, as evidenced by TEM images displayed in Figure S4. LPBF-typical α/β Ti hierarchical structures [19,53], including primary, secondary, ternary, and quaternary α' martensites, can also be observed.

3.2. Tensile properties

Fig. 5a shows the representative tensile stress-strain responses of the AP and HT samples at various temperatures. From these, mechanical properties such as YS, UTS, uniform elongation (e_u), and strain-to-failure (e_f), were extracted and are summarized in Table 3. The variations in UTS, YS, and K_{IC} with temperature are displayed in Fig. 5b, while Fig. 5c shows the variations in e_u and e_f. The AP sample exhibits high strength at RT (YS of ~ 1167.7 MPa and UTS of ~ 1281.3 MPa), similar to that reported on LPBF Ti-6Al-4V [2], which can be attributed to the presence of the fine α' martensites in the microstructure. The enhanced strength comes at the cost of ductility (e_f ~ 5.8 %). At 300 °C, a marked reduction in strength (YS ~ 881.0 MPa, UTS ~ 1037.6 MPa) coupled with a modest improvement in ductility (e_f ~ 6.9 %) were noted. Further increase of the testing temperature to 500 °C led to a smaller reduction (from that at 300 °C) in strength (YS ~ 827.5 MPa, UTS ~ 934.3 MPa), but without a complementary enhancement in ductility. Rather, a marginal reduction in ductility (e_f ~ 6.3 %) was noted. At 600 °C, significant declines in both strength (YS ~ 487.0 MPa, UTS ~ 587.2 MPa) and e_f (~ 3.8 %) were noted.

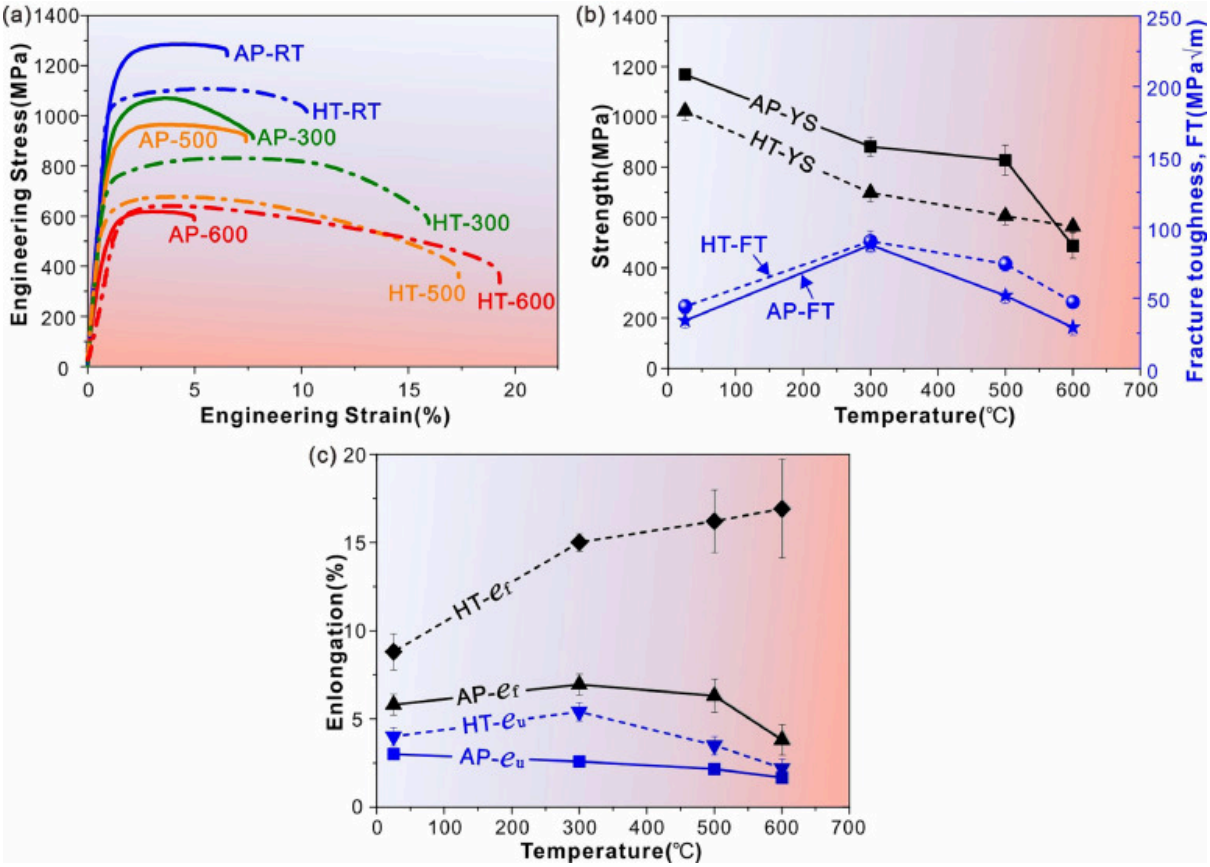

1. Download: Download high-res image (770KB)
2. Download: Download full-size image

Fig. 5. (a) Representative engineering stress-strain curves, (b) temperature dependence of UTS, YS, and K_{IC}, and (c) temperature dependence of e_u and e_f for AP and HT.

Table 3. Summary of quasi-static mechanical properties for AP and HT.

Sample	Test Temperature	YS (MPa)	UTS (MPa)	Uniform elongation e_u (%)	Strain to failure e_f (%)	Area under the tensile curve (MPa)	Fracture Toughness, K_{IC}/K_Q (MPa$\sqrt{m}$)
AP	RT	1167.7 ± 12.9	1281.3 ± 5.7	3.0 ± 0.1	5.8 ± 0.6	80.9 ± 7.1	33.9 (32.6, 35.1)
	300 ℃	881.0 ± 38.6	1037.6 ± 28.3	2.6 ± 0.2	6.9 ± 0.6	72.2 ± 5.0	87.6* (83.9*, 91.3*)
	500 ℃	827.5 ± 60.0	934.3 ± 49.3	2.2 ± 0.1	6.3 ± 0.9	80.9 ± 7.1	51.6 (49.3, 53.9)
	600 ℃	487.0 ± 50.8	587.2 ± 41.5	1.7 ± 0.1	3.8 ± 0.9	24.4 ± 4.6	29.1 (28.9, 29.3)
HT	RT	1022.3 ± 11.6	1093.7 ± 12.2	4.0 ± 0.3	8.8 ± 1.0	96.7 ± 13.7	43.9 (43.3, 44.5)
	300 ℃	697.7 ± 10.3	828.0 ± 7.9	5.4 ± 0.3	15.0 ± 0.4	118.4 ± 2.7	90.3* (85.1*, 95.4*)
	500 ℃	606.0 ± 17.7	692.3 ± 17.5	3.5 ± 0.3	16.2 ± 1.8	102.6 ± 8.4	74.2* (71.9*, 76.5*)
	600 ℃	563.7 ± 20.7	637.7 ± 1.5	2.2 ± 0.1	16.9 ± 2.8	94.8 ± 15.7	47.1[#]

*Plane strain conditions, as per ASTM E399, were not satisfied.

[#]Single replicate test due to insufficient samples, caused by the limited build plate size and hence, the batch size.

As expected, heat treatment led a decrease in strength (YS ~ 1022.3 MPa, UTS ~ 1093.7 MPa) at RT, accompanied by a significant improvement in e_f (to ~ 8.8 %). Similar to that observed in the AP state, HT samples exhibit a decrease in strength at elevated temperatures, with YS ~ 697.7 MPa and UTS ~ 828.0 MPa at 300 °C. Furthermore, at 500 °C, the values are YS ~ 606.0 MPa and UTS ~ 692.3 MPa, while at 600 °C, they further decrease to YS ~ 563.7 MPa and UTS ~ 637.7 MPa. What distinguishes HT from AP at elevated temperatures is the superior e_f responses, along with the absence of e_f dip up to 600 °C. For instance, there is a noteworthy 97.5 % increase (19 % in the case of AP) in e_f from RT to 300 °C, resulting in an e_f of ~ 15.0 % at 300 °C. This is followed by a marginal increment in e_f to ~ 16.2 % at 500 °C, and further to ~16.9 % at 600 °C.

Postmortem analyses of the polished side surfaces of the tensile specimens near the fracture surface, as shown in Fig. 6, revealed distinct fracture behaviors of the AP and HT samples. In the AP samples, void nucleation along prior β boundaries that becomes more prominent with increasing test

temperature is noted. The formation of voids is accompanied by the appearance of β phase precipitation along the prior β boundaries in AP-600. Postmortem TEM analyses of AP-300, AP-500, and AP-600 tensile fractured specimens (taken from the uniformly elongated locations, far away from the fracture surface) further confirmed the occurrence of α' decomposition and β phase precipitation along the grain boundaries in samples tested at both 500 and 600 °C, as illustrated in Figs. 7d-f and g-i, respectively. The nano-sized β phase, with dimensions of approximately 3 nm in AP-500, are too small to be observed with SEM. The presence of the β stabilizer element, Mo, in these nano-β ligaments after deformation at 500 °C, was detected through STEM-EDX analysis (Fig. 7f). The presence of the nano-sized β ligaments after deformation at 600 °C was confirmed via SAED (Fig. 7i), with larger width of ~30 nm, and additionally ~70 nm sized β phase along the high-angle prior-β grain boundaries (Fig. 6d). Note that similar nano-β ligament formation was also observed in Figs. 7j-l and Figure S5, after exposure to 600 °C in the undeformed regions. However, there was no size disparity between those within the prior β grains and on the grain boundaries. This indicates that strain at high temperatures facilitates the diffusion of Mo and hence, growth of that β ligaments that are located at the prior β boundaries. In contrast, decomposition of α' is minimal in AP-300, as indicated by the negligible Mo segregation (Fig. 7c). This finding suggests that the diffusion kinetics at 500 °C and above are sufficiently high, especially along high-angle prior-β grain boundaries, which facilitate stress-induced void nucleation that is enhanced by diffusion. By corollary, the absence of void nucleation at 300 °C is attributed to the slower diffusion kinetics at that temperature. This transition temperature aligns with prior literature that indicates the occurrence of α' decomposition in Ti-6Al-4V above 400 °C [47].

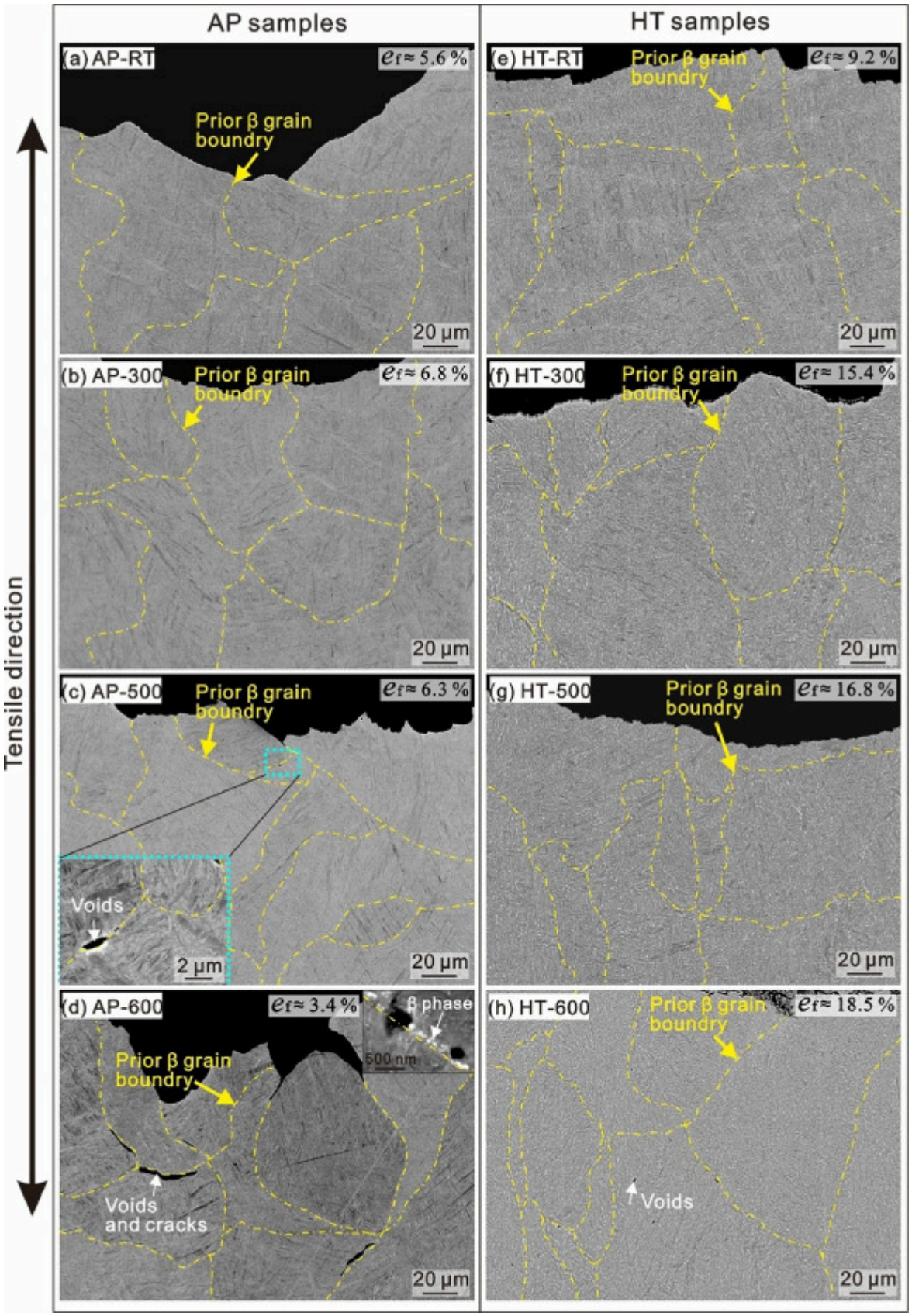

1. Download: Download high-res image (2MB)
2. Download: Download full-size image

Fig. 6. Postmortem analysis on the polished side surface of tensile fractured (a-d) AP and (e-h) HT,

tested at (a, e) RT, (b, f) 300 °C, (c, g) 500 °C, and (d, h) 600 °C.

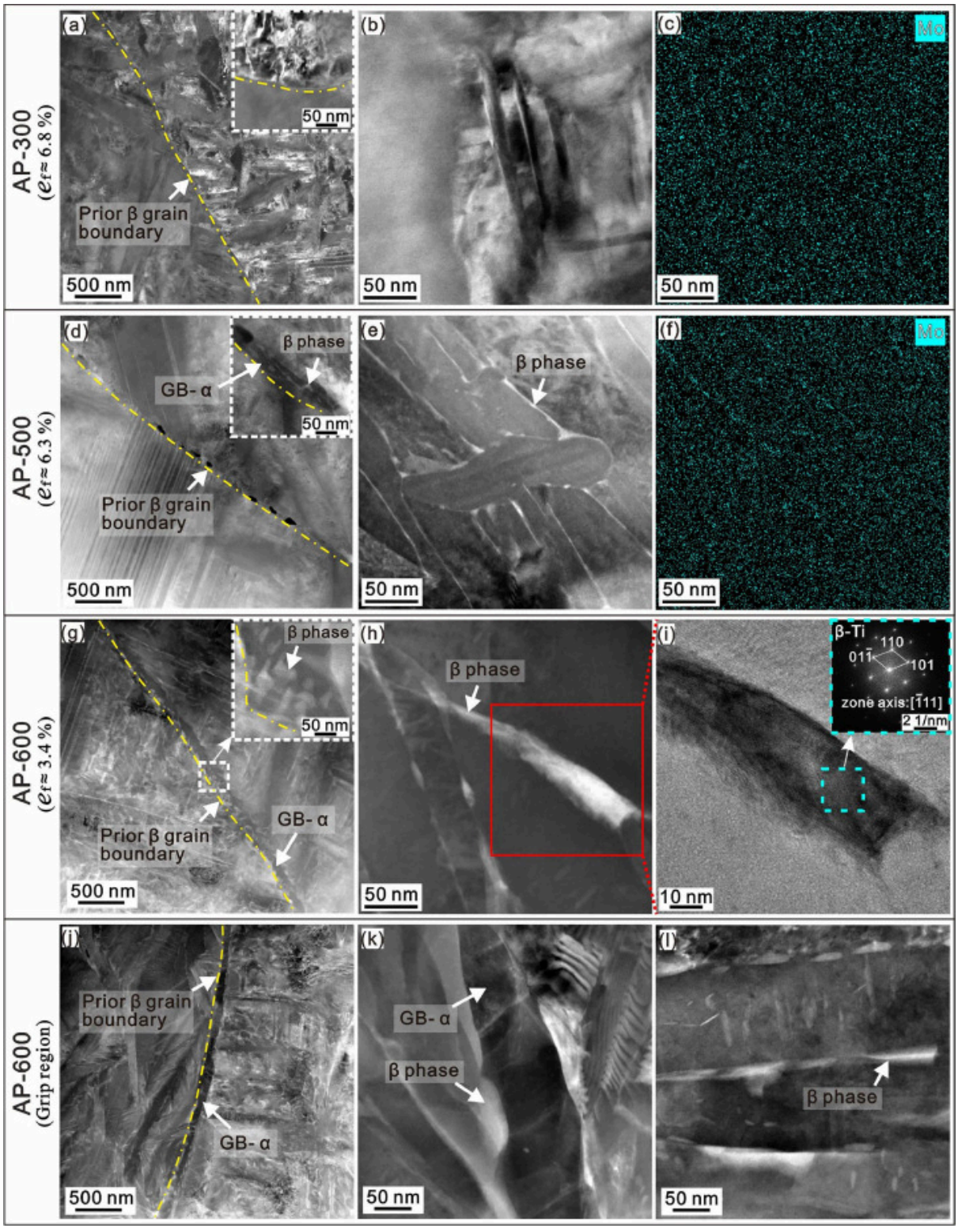

1. Download: Download high-res image (3MB)
2. Download: Download full-size image

Fig. 7. Postmortem TEM analysis of (a-c) AP-300, (d-f) AP-500, and (g-i) AP-600 samples at regions with uniform elongation, and (j-l) AP-600 samples from the grip section (without deformation): (a-b, d-e, g-h, j-l) HAADF images at different magnifications. (c) and (f) correspond to the STEM-EDX of (b) and (e).

(i) HR-TEM of the highlighted region in (h), with inset showing the SAED pattern of β phase.

Observations made on the side surfaces of the tensile tested HT samples indicated minimal voids. Moreover, there appears to be no specific preference for the nucleation of the few that were observed (Figs. 6e-h). This stark contrast in the preferential sites of void nucleation between the AP and HT samples offers a rationale for the early failure observed in the AP samples at elevated temperatures. This phenomenon further substantiates HT samples' improvement in e_f upon the increase in the test temperature from 300 to 600 °C, which is in contrast to the deterioration observed in the AP state. In particular, void nucleation along prior β boundaries is ubiquitous in AP-600, whereas it could be hardly observed in HT-600.

Results of the postmortem TEM analyses of HT-300, HT-500, and HT-600, as well as untested HT, are shown in Fig. 8. The microstructure of the samples remains unchanged, even after high-temperature tests. This is because the testing temperatures are well below the aging temperature of 800 °C. The observation of β-ligament evolution in AP and HT samples at different test temperatures provides a rationale for the observed trend in YS. The high-temperature strength of β Ti is known to be inferior to that of α Ti [54]. Hence, YS of AP samples sharply drops (by ~41 %) between 500 and 600 °C, due to the significant in-situ precipitation of the β phase at 600 °C. In contrast, the HT samples exhibit a more gradual reduction in strength due to the stable microstructure within the test temperature range.

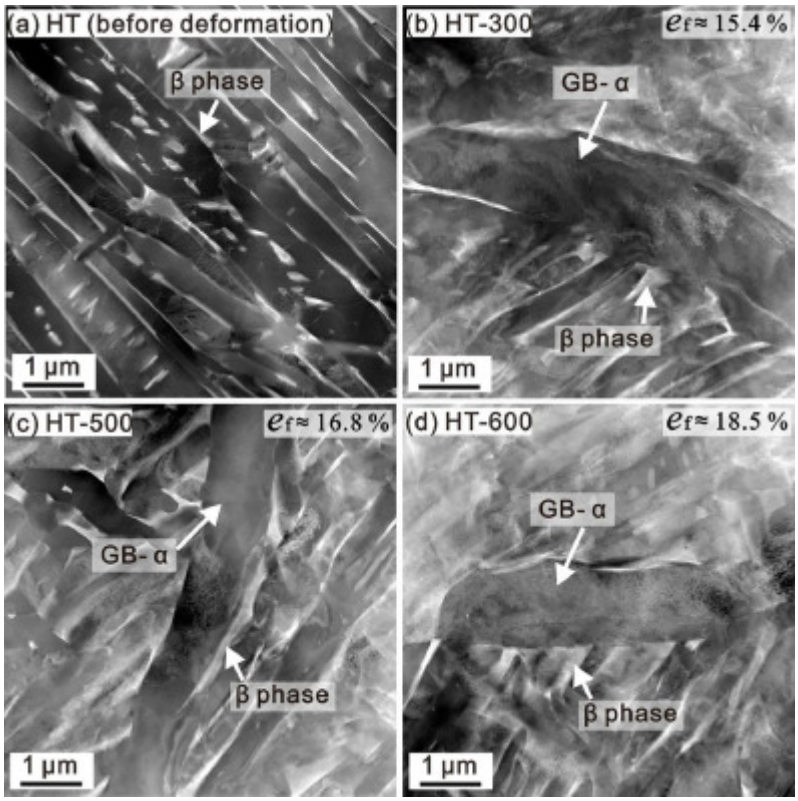

1. Download: Download high-res image (644KB)
2. Download: Download full-size image

Fig. 8. TEM-HAADF analysis of (a) HT (before deformation), (b) HT-300, (c) HT-500, and (d) HT-600 samples at regions with uniform elongation.

3.3. Fracture toughness

To investigate the influence of temperature and heat treatment on fracture toughness, K_{IC} was experimentally assessed for both AP and HT samples under different temperature conditions, and the

results are provided in Table 3. Representative load versus crack mouth opening displacement (CMOD) data is given in Figure S6, illustrating predominantly linear loading characteristics until fracture. Note that the AP samples tested at 300 °C as well as the HT ones tested at 300 and 500 °C do not satisfy the plane strain conditions, as specified by the ASTM standard E399–23 [45]. Nevertheless, the largest estimated plane strain plastic zone size (1.78 mm in HT-300) is only about one-seventh of the specimen thickness (B). This aligns with findings in a prior study on Ti-6Al-4V (see Footnote 1 in the paper) [3], where the conditional fracture toughness (K_Q) values were deemed close to the K_{IC} values for samples exhibiting linear loading characteristics. As a result, the comparison of fracture toughness will be conducted across all material testing conditions using K_Q/K_{IC} values.

The AP sample exhibited a low fracture toughness of 33.9 MPa√m at RT, which is consistent with the material's limited ductility. This value significantly improves to around 87.6 MPa√m at 300 °C, but then declines by 41.1 % to 51.6 MPa√m at 500 °C and drops further by 43.6 % to 29.1 MPa√m at 600 °C, which is even below that at RT. A similar trend is observed for the HT samples, with an increase from 43.9 MPa√m at RT to 90.3 MPa√m at 300 °C, followed by a 17.8 % decrease to 74.2 MPa√m at 500 °C and a further 36.5 % decline to 47.1 MPa√m at 600 °C. Overall, the deterioration of fracture toughness from 300 to 600 °C is far less pronounced for the HT samples. Given the similar tensile responses of HT-500 and HT-600, external factors such as oxygen and moisture are the most probable sources that induce embrittlement at 600 °C. By increasing the temperature from 500 to 600 °C, it was shown that the oxygen uptake due to the formation of oxide and diffusion into the material can be an order of magnitude higher for Ti-6Al-4V [33], thereby causing significant embrittlement of an α/β Ti alloy.

Representative fractographs corresponding to each sample, obtained from the fractured region immediately ahead of the fatigue pre-crack tip, are displayed in Fig. 9, with a higher magnification image shown in Figure S7. These images reflect the fracture toughness characteristics. For instance, the AP-RT sample (having poor fracture toughness ~33.9 MPa√m) exhibits a relatively flat fracture morphology (Fig. 9a). While AP-600, HT-RT and HT-600 exhibit corrugated fracture morphologies, shown respectively in Figs. 9d, e and h, their fracture surfaces resemble either cleavage fracture patterns (Figures S7 d and e, for AP-600 and HT-RT, respectively) or quasi-cleavage fractures with shallow dimples (Figure S7 h for HT-600), corresponding to their lower fracture toughness (<47.1 MPa√m). In contrast, all the samples with fracture toughness values exceeding 51.6 MPa√m (AP-300, HT-300, AP-500, and HT-500) display both corrugated fracture morphology (Figs. 9b, f, c, and g, respectively) and deep dimpled surfaces (Figures S7 b, f, c, and g, respectively), indicative of a ductile failure mode. The corrugation features on the surfaces align well with the length scale of the prior β grains.

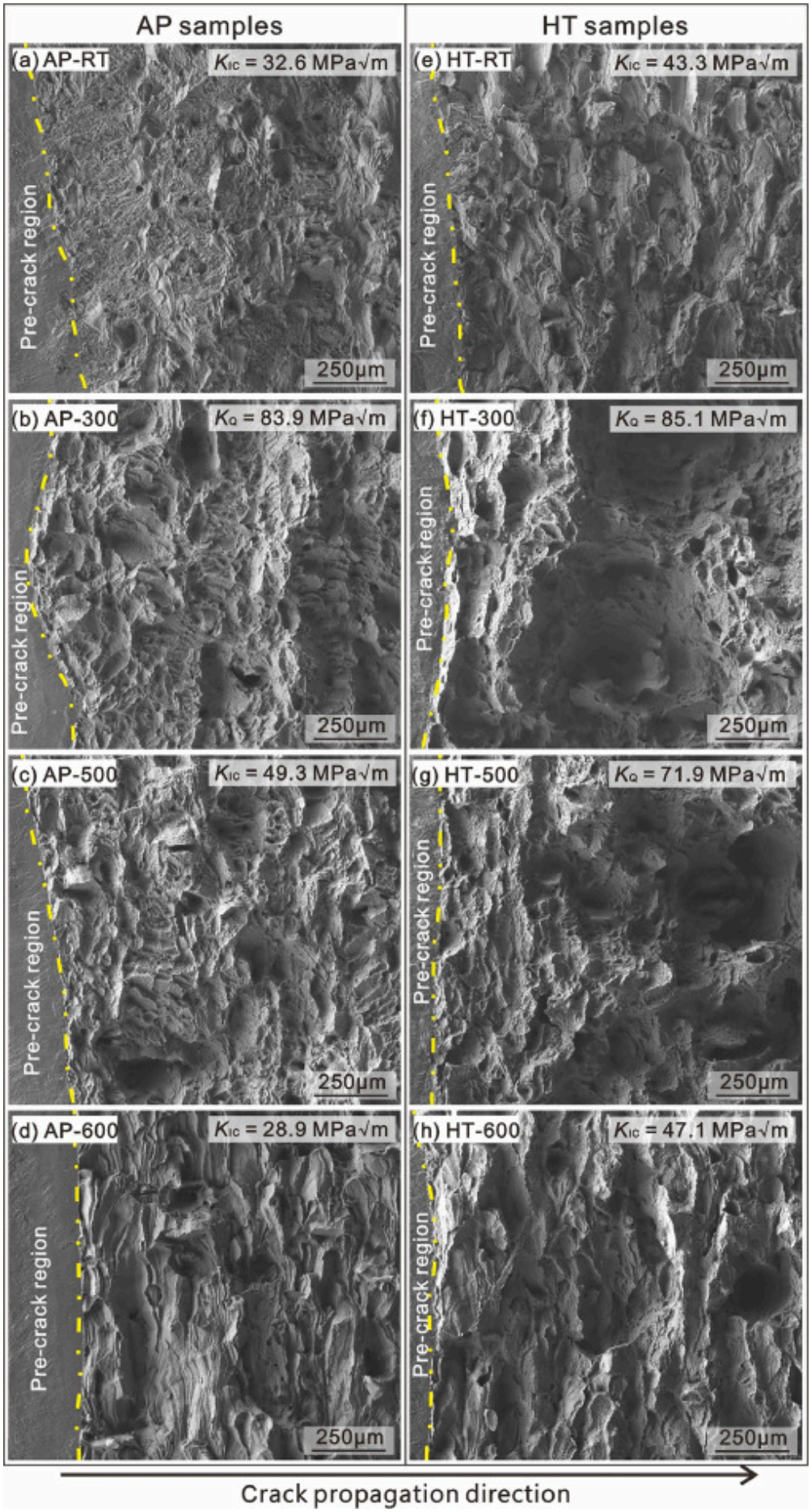
AP samples
HT samples
(a) AP-RT
K_{IC} = 32.6 MPa√m
(e) HT-RT
K_{IC} = 43.3 MPa√m
(b) AP-300
K_Q = 83.9 MPa√m
(f) HT-300
K_Q = 85.1 MPa√m
(c) AP-500
K_{IC} = 49.3 MPa√m
(g) HT-500
K_Q = 71.9 MPa√m
(d) AP-600
K_{IC} = 28.9 MPa√m
(h) HT-600
K_{IC} = 47.1 MPa√m
Pre-crack region
250μm
Crack propagation direction

1. Download: Download high-res image (2MB)
2. Download: Download full-size image

Fig. 9. Representative fractographs of (a-d) AP and (e-h) HT, tested at (a, e) RT, (b, f) 300 °C, (c, g) 500 °C, and (d, h) 600 °C.

The side surfaces of the C(T) specimens were polished postmortem and observed at locations immediately ahead of the fatigue crack tip and below the fracture surface, as illustrated in Fig. 10. The observed features closely resemble those made on the side surfaces of the tensile tested specimens (Figs. 6a-d for AP and Figs. 6e-h for HT). Significant void nucleation is apparent in both AP-500 and AP-600 along the prior β grain boundaries (More SEM observations of prior β boundary void nucleation in AP-600 can be made from Figures S8). In contrast, HT-300, HT-500, and HT-600 exhibit fine and spherical void formation away from the fractured surface. While multiple voids are present, they are relatively small (~0.7 μm) and rounded, and do not appear to occur only along the prior β boundaries. Thus, the distributed void formation in these cases does not appear to facilitate crack propagation along the prior β grain boundaries.

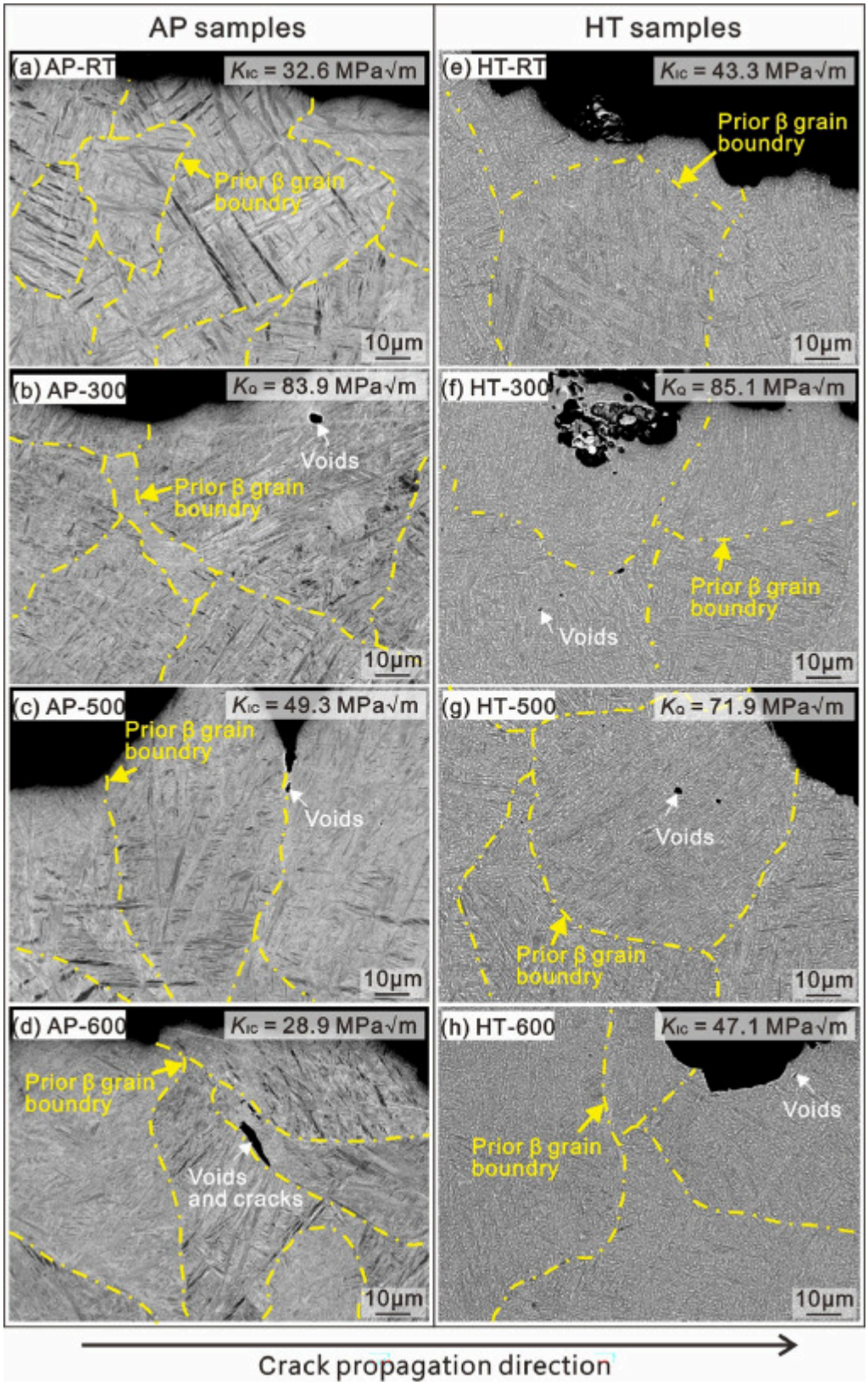

1. Download: Download high-res image (3MB)
2. Download: Download full-size image

Fig. 10. Observation of overload fractures in (a-d) AP and (e-h) HT, taken from the polished side surface at the middle section (plane-strain region) of C(T) specimens. Tests were performed at different

temperatures: (a, e) RT, (b, f) 300 °C, (c, g) 500 °C, and (d, h) 600 °C.

3.4. Fatigue crack growth

The FCG rates as a function of ΔK, measured at different temperatures, are presented in Figs. 11a and b for AP and HT samples, respectively. Additionally, the FCG curves for AP and HT at RT, 300, 500, and 600 °C are plotted respectively in Fig. 11c-f, to facilitate easy comparison. The values of m and ΔK_o, estimated from such plots, are summarized in Table 4. Irrespective of whether it is AP or HT, an increase in temperature resulted in a deterioration of FCG resistance within the Paris regime. This is evident in the upward shift of the curves with increasing temperature. Meanwhile, the m values of both the AP and HT samples decrease with increasing temperature, to the degree that they fall outside the typical range of 2–4 (common for most metals at room temperature [55]) at 500 and 600 °C, which is a desirable characteristic as it indicates a slower acceleration in crack growth rate with increasing ΔK. Additionally, at elevated temperatures, the m value of the AP sample consistently remains lower than that of the HT sample.

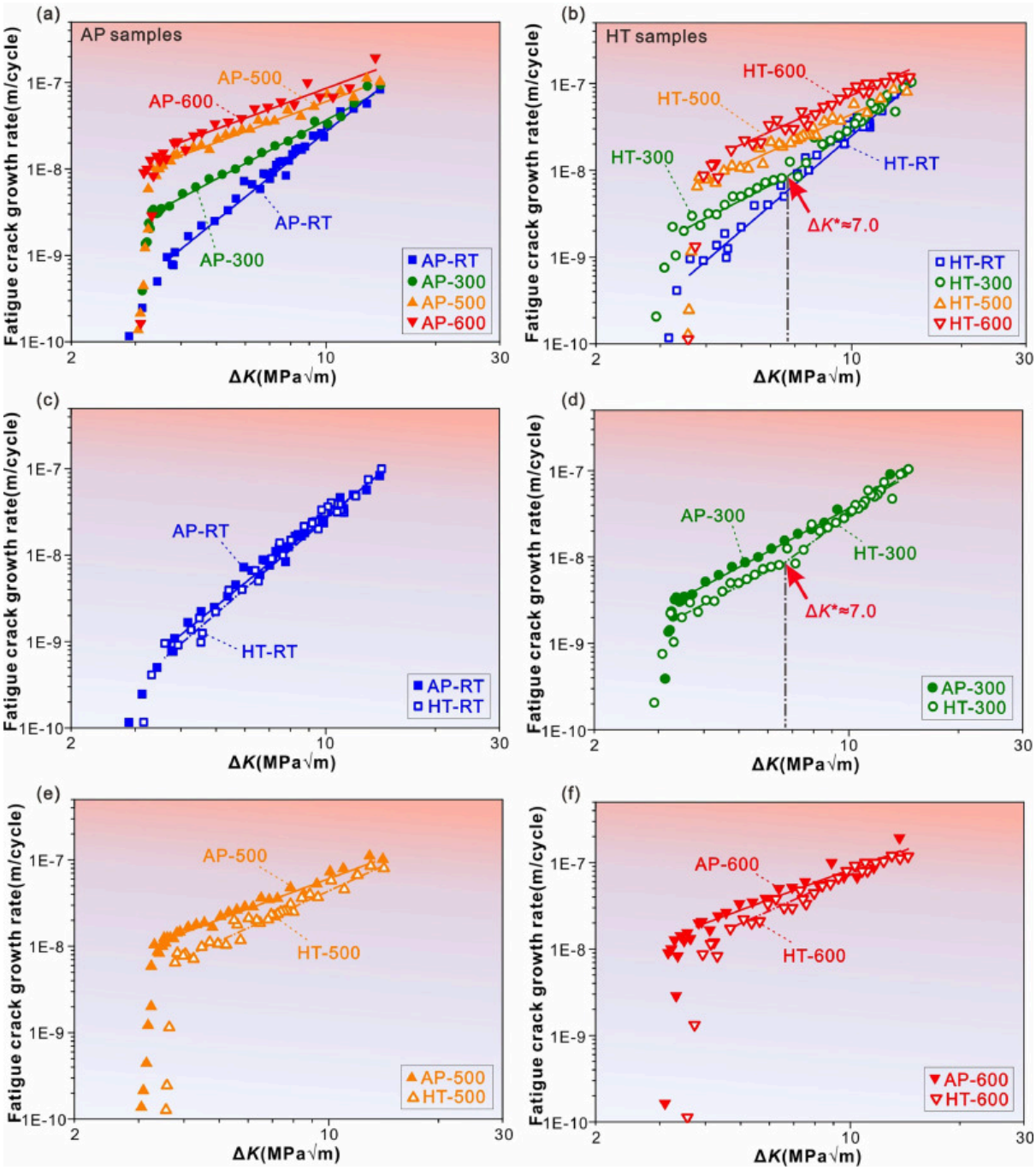

1. Download: Download high-res image (2MB)
2. Download: Download full-size image

Fig. 11. Representative FCG behaviors for (a) AP and (b) HT. (c-f) are sub-figures for the comparison of FCG characteristics at a single test temperature: (c) RT, (d) 300 °C, (e) 500 °C, and (f) 600 °C.

Table 4. Summary of FCG properties for AP and HT.

Sample	Temperature	*m*	ΔK_o (MPa√m)	r_c at ΔK_o (um)	$\Delta K_{T\beta}$ (MPa√m)	$\Delta K_{T\alpha}$ (MPa√m)
AP	RT	3.4 (3.3, 3.4)	2.7 (2.5, 2.9)	0.1	86.5	9.3
	300 ℃	2.3 (2.3, 2.3)	3.0 (3.1, 2.8)	0.3	65.3	7.1

Sample	Temperature	*m*	ΔK_o (MPa√m)	r_c at ΔK_o (um)	$\Delta K_{T\beta}$ (MPa√m)	$\Delta K_{T\alpha}$ (MPa√m)
	500 ℃	1.6 (1.5, 1.6)	3.1 (3.0, 3.1)	0.4	61.3	6.6
	600 ℃	1.5 (1.5, 1.5)	3.2 (3.1, 3.3)	1.1	36.1	3.9
HT	RT	3.8 (3.6, 3.9)	3.4 (3.2, 3.5)	0.3	78.5	8.4
	300 ℃	3.1 (3.0, 3.1), 2.2 (2.1, 2.3)	3.0 (3.0, 2.9)	0.5	53.6	5.7
	500 ℃	2.0 (1.9, 2.0)	3.6 (3.6, 3.5)	0.9	46.5	5.0
	600 ℃	1.7 (1.6, 1.8)	3.7 (3.6, 3.7)	1.1	43.3	4.6

Fig. 12 shows representative FCG paths obtained with a relatively high ΔK of ~15.5 MPa√m (all in the Paris regime) from samples tested at different temperatures. An overall crack tortuosity is evident in all samples, with crack deflection that correlates with the α/α' lath microstructure. Additionally, secondary cracks appear to form along the α/α' lath boundaries, with their amount and length increasing with temperature. This often led to crack deflection or even bifurcation. Notably, the phenomena of secondary crack formation and bifurcation are more prominent for HT samples tested at 300, 500, and 600 °C. This indicates that the inter-lath region with β phase has a higher tendency to crack, which contrasts with what is observed under the quasi-static loading conditions.

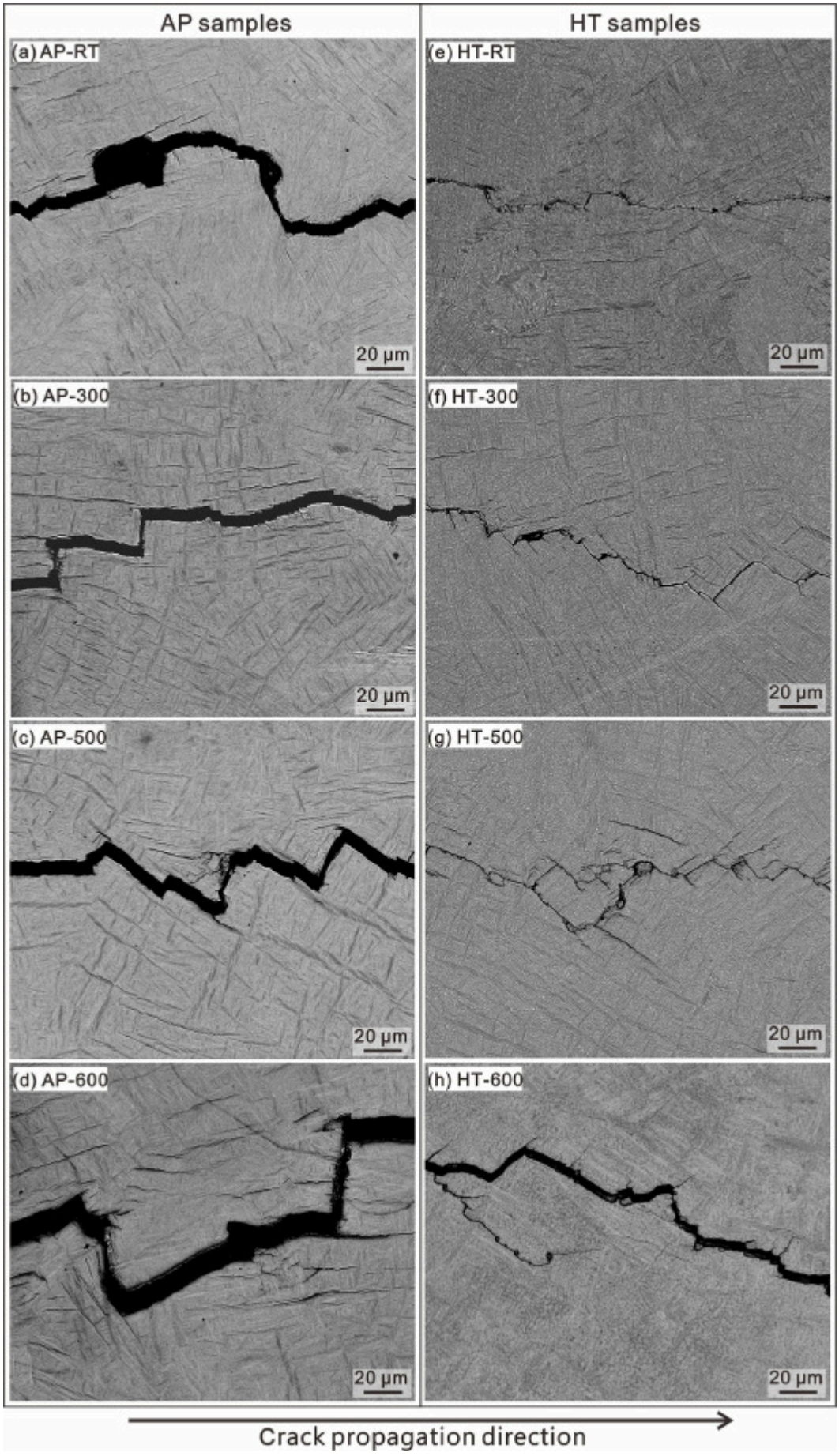
AP samples
HT samples
(a) AP-RT
(e) HT-RT
(b) AP-300
(f) HT-300
(c) AP-500
(g) HT-500
(d) AP-600
(h) HT-600
20 μm
Crack propagation direction

1. Download: Download high-res image (3MB)
2. Download: Download full-size image

Fig. 12. Representative FCG characteristics at high ΔK (~15.5 MPa$\sqrt{m}$) for (a-d) AP and (e-h) HT, tested at (a, e) RT, (b, f) 300 °C, (c, g) 500 °C, and (d, h) 600 °C.

Despite the deteriorating FCG behavior in the Paris regime with increasing temperature, ΔK_o either remained invariant or marginally improved with temperature. For the AP samples, ΔK_o remain within the same range for all temperatures, and gradually—but marginally—improve from 2.7 MPa$\sqrt{m}$ at RT to 3.2 MPa$\sqrt{m}$ at 600 °C. However, for HT, ΔK_o first decreased (from 3.4 MPa$\sqrt{m}$ at RT to 3.0 MPa$\sqrt{m}$ at 300 °C) and then increased again (to 3.6 MPa$\sqrt{m}$ at 500 °C and 3.7 MPa$\sqrt{m}$ at 600 °C). Its value at HT-300 stands out, in addition to being the only case where a distinct change in crack growth rates within the Paris regime, with a "kink" at a ΔK of ~7.0 MPa$\sqrt{m}$, occurs. This anomaly is discussed in a later section.

Subsequent crack observations were performed at the near-threshold regime (corresponding to ΔK_o), as shown in Fig. 13, to gain a better understanding of the trends observed in ΔK_o – temperature data. In both the AP and HT conditions, higher temperatures resulted in less serrated crack growth, yet yielded improved resistance to FCG within the threshold regime in all the specimens (except HT-300). This trend might initially seem counterintuitive, as FCG in the threshold regime is commonly associated with the interaction of the crack tip with the local microstructure, leading to serrated crack growth and a slowing of FCG [55]. Nevertheless, elevated temperatures also led to crack tip blunting (except HT-300). The blunting condition of crack tips correlates well with the changes in ΔK_o. Since the experiments were performed in an open environment, oxidation at elevated temperatures cannot be disregarded. One cannot solely attribute the counterintuitive improvement in threshold crack growth behavior to just blunting, but also consider oxidation, which will be further investigated in the subsequent discussion. Another noteworthy observation is that HT samples at 300, 500, and 600 °C exhibit more serrated growth and bifurcation compared to their AP counterparts at the same temperatures. Together with the observation of FCG at high ΔK values, shown previously in Fig. 12, where HT samples show a higher occurrence of secondary cracks, it appears that the inter-lath β phase plays a key role in facilitating fatigue crack behavior near-threshold as well as in the Paris regime at elevated temperatures.

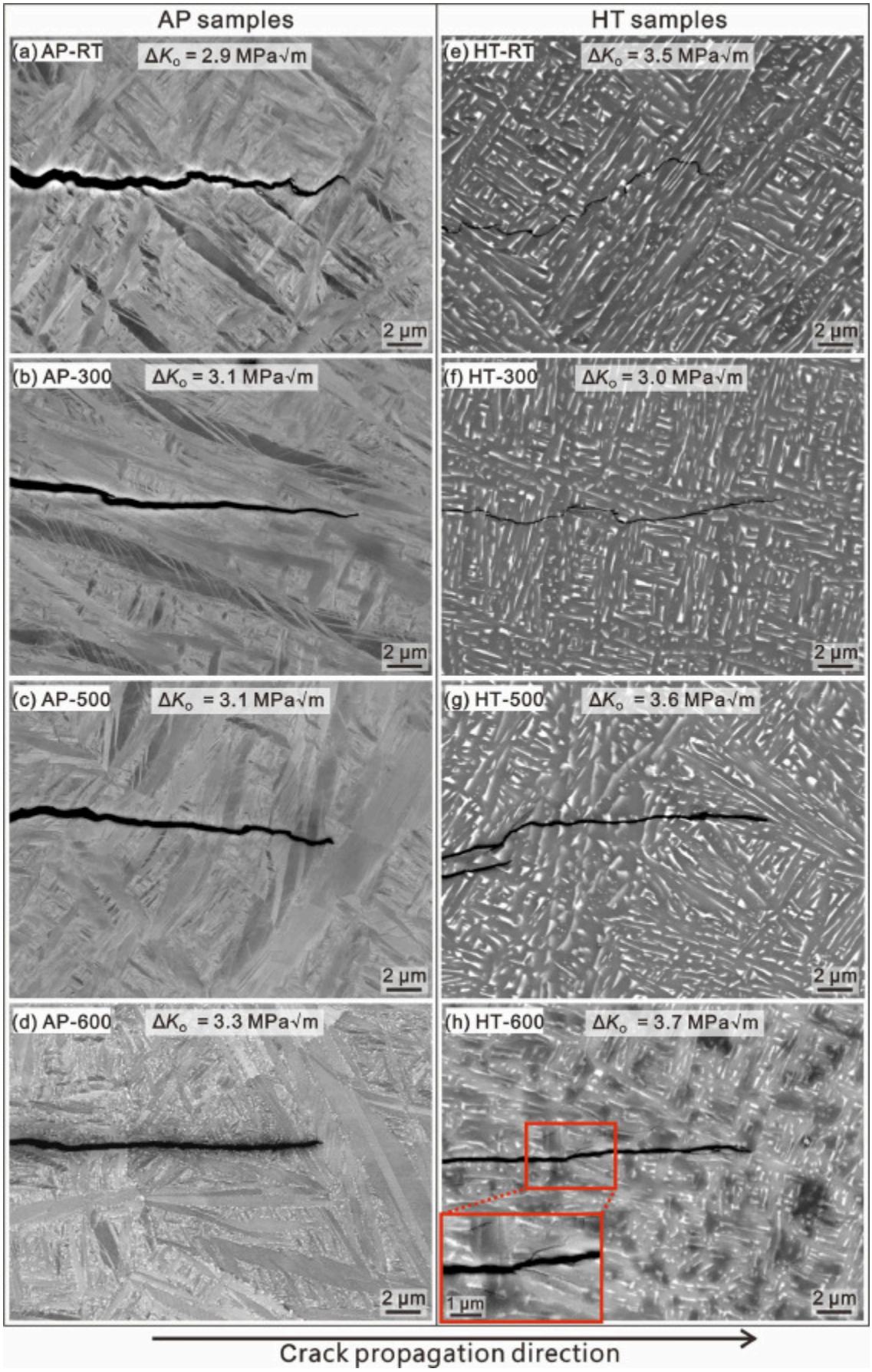

1. Download: Download high-res image (2MB)

2. Download: Download full-size image

Fig. 13. Representative near-threshold FCG characteristics for (a-d) AP and (e-h) HT, tested at (a, e) RT, (b, f) 300 °C, (c, g) 500 °C, and (d, h) 600 °C.

4. Discussion

The postmortem investigations show the damage mechanisms in the AP and HT conditions to be distinct, with the β ligament absent in the former and present in the latter due to α' decomposition. In this section, we will delve further into how β phase can play a key role in influencing the fracture and fatigue behavior at elevated temperatures in an α/β Ti alloy.

4.1. The role of β phase on void nucleation and growth

At elevated temperatures, the quasi-static fracture behavior of the alloys under investigation is influenced by the stress-induced void formation, which, in turn, is affected by the microstructural differences in AP and HT conditions. As previously mentioned, exposure of the alloy to temperatures above 400 °C results in the transformation of the α' phase into α+β phases, which is diffusion-driven [47]. To verify this transformation's applicability to the alloy of the present study, TEM was performed on samples obtained from the fracture-tested samples of AP-300, AP-500, and AP-600. As shown in Fig. 7, β ligaments are observed in those tested above 400 °C. They are notably absent in AP-300, even in the presence of high strain, which should facilitate diffusion. It is worth noting that the diffusion kinetics are likely to be significant at temperature ≥ 500 °C, as indicated by the distinct β ligament formation, even though these tests commence after only ~15 min of soak time.

With sufficiently fast diffusion kinetics, stress-induced creep cavitation and growth can occur at elevated temperatures [56]. Both prior β grains and α boundaries act as dislocation barriers, potentially facilitating void nucleation through the grain boundary sliding, vacancy condensation, or the Zener-Stroh mechanism [56]. In the work reported hitherto, prior β grains were consistently identified as the primary sites for such cavitation during the creep tests, especially in Ti alloys with lamellar or Widmanstätten microstructures (with β ligaments), eventually leading to crack formation. This phenomenon has been observed across different titanium alloys and temperatures in creep tests. For example, in Ti-6Al-4V at 455 °C [57] and 600 °C [58], as well as Ti-1100 at 600 °C [59]. Meanwhile, in the case of Ti-5Zr-0.5Si tested at 538 °C, grain boundary sliding was prominent and primarily occurred along the prior β grain boundaries [60]. These observations of prior β grain boundaries being preferential sites for damage nucleation and propagation is in agreement with the observations made on the AP samples (despite the fact that the tests conducted in the present study are not creep experiments), suggesting that creep-related mechanisms dominate the cavitation process. In the AP samples, cavitation is primarily observed along prior β grain boundaries when loaded above the aforementioned threshold temperature of 400 °C, as shown in Figs. 6c and d.

However, in the HT samples where β ligaments are uniformly distributed throughout the material, cavities were hardly observed near the fracture surface of the tensile specimens tested at 500 and 600 °C, as shown in Figs. 6g and h, respectively. Meanwhile, in the C(T) specimens, cavity formation was distributed and not limited solely to the prior β boundaries, as shown in Figs. 10g and h for 500 and 600 °C testing condition, respectively. It is important to mention here that the observations on the fracture toughness tested specimens were made at the mid-thickness of the C(T) specimens. Hence, a triaxial stress state that promotes cavity formation should be predominant in those regions [61]. We infer that the observed characteristic of distributed cavity formation (in the case of C(T) specimens) is beneficial for toughening the alloy because of the following reason. When voids nucleate preferentially along the prior β boundaries, the spacing between neighboring cavities becomes closer

compared to the cases where cavities are well distributed. The reduced cavity spacing (that eventually develops into crack like morphology) results in a significantly lowered resistance for crack propagation [38,[62], [63], [64]], and hence, lower toughness.

In the above context, the role of β phase, which is recognized as "soft" (in comparison to the α phase) [65,66], requires some closer examination. Prior investigations using in-situ synchrotron X-ray diffraction on the α/β Ti-Al-V-Fe-Si-O alloy tensile tested at RT have highlighted the significant role played by the β phase (predominant β lattice expansion beyond yield) in accommodating higher levels of strain [67]. The presence of β ligaments in the microstructure facilitates strain accommodation and distribution. (The thin morphology of the β phase observed in this study makes it difficult to be indexed via EBSD.) It is also important to note that the β phase, in which the self-diffusion rate is two orders of magnitude higher than that in α [43], can effectively promote creep and relaxation through dislocation climb at elevated temperatures, even during the relatively short duration of tensile and fracture toughness tests. This action significantly delays the formation of creep cavities in HT-500 and HT-600, in contrast to AP-500 and AP-600, as demonstrated by the lack of observable cavities in the tensile tested samples. Otherwise, the presence of cavities would have exerted a detrimental influence on the uniaxial tensile ductility and the fracture toughness, as evident from Table 3. In this regard, it would be valuable to investigate the fracture behavior anisotropy at elevated temperatures, considering the formation of columnar prior β grains in the LPBF α/β Ti alloy and the preferential void nucleation at their grain boundaries observed in the AP-500 and AP-600 samples.

Given the possibility of nanoscale β phase precipitation during the tensile testing of AP-500 and AP-600, its possible role on the preferential void nucleation at the prior β grain boundaries should also be probed, as strain incompatibility and stress concentration have been reported at the α/nano-β phase boundaries [23,68]. As mentioned earlier, TEM analysis of the AP sample before testing (Figure S4) and AP-500/AP-600 after testing (Fig. 7) demonstrates that the nano-β ligaments at α lath and prior β boundaries can form after only a brief (~15–30 min, 15 min preheat and less than 15 min test time) exposure to 500/600 °C. This prompted us to conduct a tensile test at RT on an AP sample that was heat treated *a priori* at 600 °C for 15 min. (TEM analysis on it, prior to testing, showed the formation of nano-β formation, Figure S9.) This test was performed to critically examine the roles of high temperature diffusion and creep. The representative tensile curve is shown in Fig. 14a, elucidating a severely embrittled sample, with e_f ~2.8 %, due to the nano-β precipitation. It was also observed that void nucleation occurred within prior β grain boundaries rather than on them, as shown in Figs. 14b and c. This provides further support that preferential void nucleation at the prior β boundaries is aided by creep cavitation in AP-500 and AP-600, and not by the strain localization within the nano-β ligaments alone.

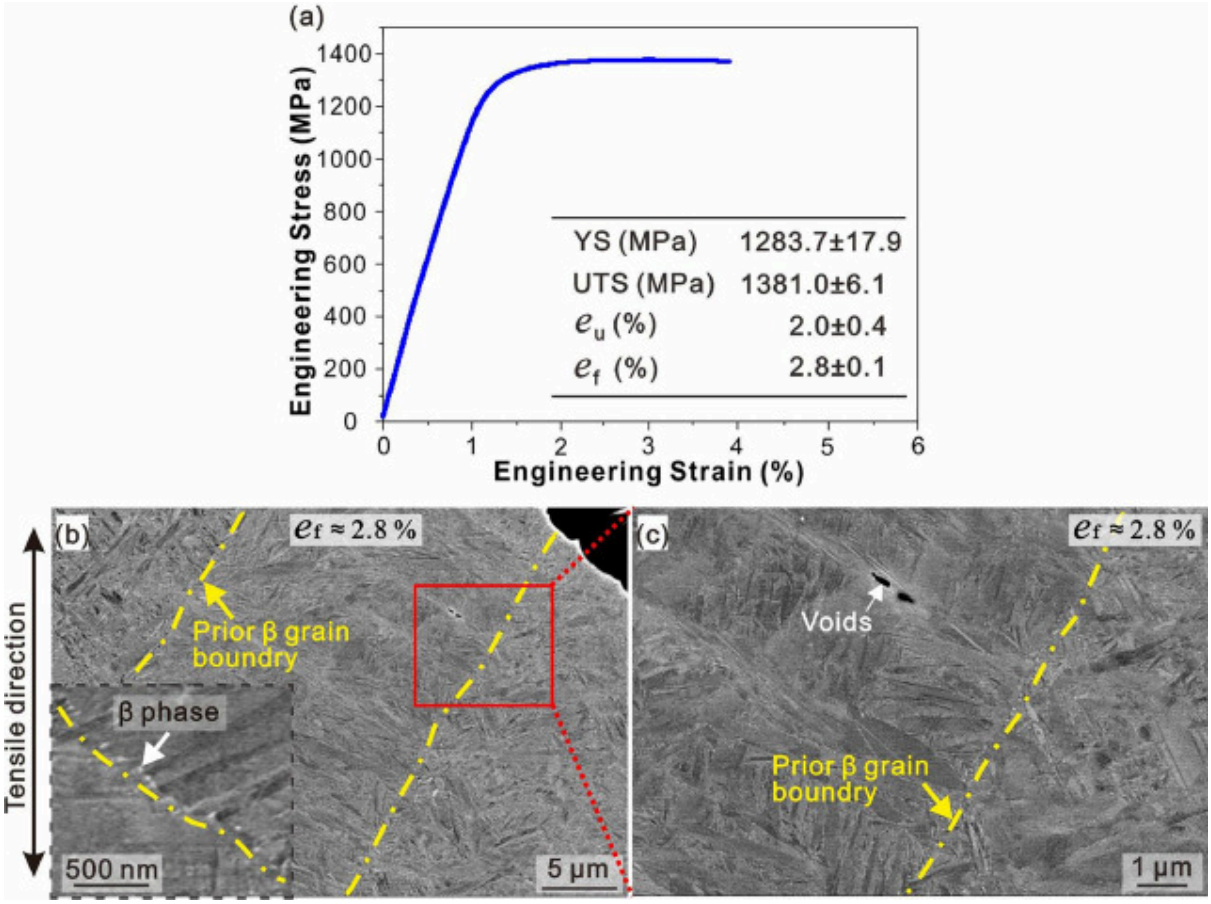

1. Download: Download high-res image (993KB)
2. Download: Download full-size image

Fig. 14. (a) Tensile response and (b) void nucleation characteristics of AP sample exposed to 600 °C for 15 min and tested at RT.

Another hypothesis for void nucleation at the prior β grain boundaries in AP-500 and AP-600 is related to grain boundary α precipitation and growth (along the prior β grain boundaries) after brief exposure to 500 and 600 °C, as observed in Fig. 7d and g, respectively. Grain boundary α could lead to strain localization and cracking along its boundary in the Ti alloys [69], which is particularly problematic in the β Ti alloys as they would lead to the formation of a precipitate-free zone and hence a softer phase [70], with continuous grain boundary α being more detrimental than discontinuous grain boundary α [71]. To address this aspect, a comparison of the grain boundary α formation at prior β boundaries of AP-500, AP-600, HT-500, and HT-600 is made in Fig. 15. The grain boundary α in AP-500 and AP-600 is thin (~50–200 nm) with discontinuous morphology in AP-500. In contrast, it is much thicker (~1–2 μm) in HT-500 and HT-600. Despite the substantial formation of continuous grain boundary α in HT-500 and HT-600, void nucleation along prior β grain boundaries was not observed. This rules out the possibility of in-situ grain boundary α formation being dominant in the prior β boundary void nucleation in HT-500 and HT-600.

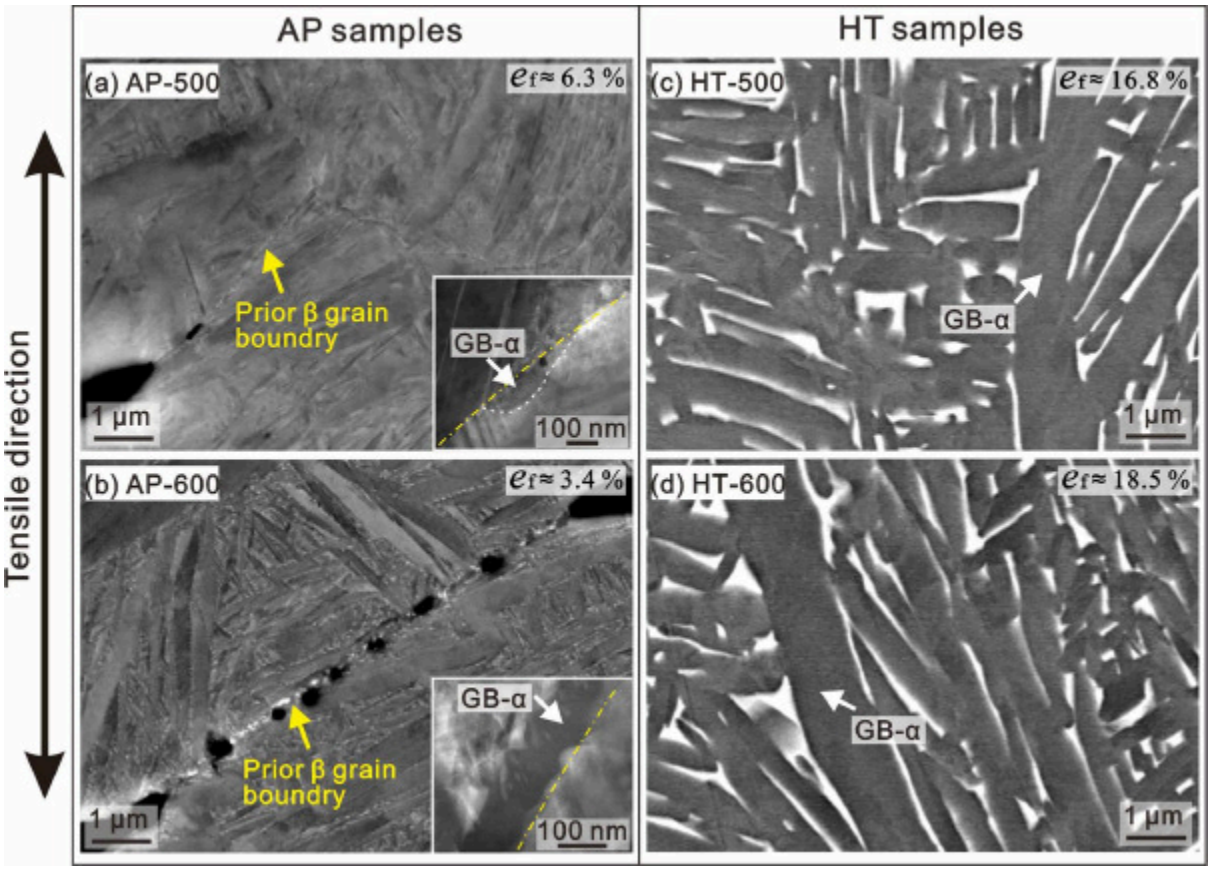

1. Download: Download high-res image (956KB)
2. Download: Download full-size image

Fig. 15. SEM images showing the grain boundary morphology for AP (a, b) and HT (c, d) after tensile testing at 500 °C and 600 °C. The inset in (a) and (b) presents TEM-HAADF images.

Furthermore, pre-existing dislocations can significantly affect the high-temperature mechanical behavior of Ti alloys, by promoting diffusion and enhancing creep [72]. As mentioned previously, a high density of dislocations is observed in the AP samples throughout the microstructure. They could enhance the precipitation and diffusion kinetics and thus influence void formation at high temperatures. Despite this, the prior β grain boundary remains a critical site for diffusion when strained, as evidenced by the larger β precipitates observed along these boundaries (Fig. 6d and Fig. 15b), in contrast to those within, after brief exposure to 600 °C, as shown in Figs. 7j-l and Figure S5. This underscores the role of prior β grain boundaries in promoting diffusion and hence creep cavitation.

4.2. The role of β phase on fatigue crack growth behavior

A worsening of the FCG behavior at high temperatures in Ti alloy has been reported in prior studies; it has been largely attributed to oxygen effects [73,74]. Beyond 300 °C, titanium experiences a significant enhancement in the dissolution of oxygen into it, leading to a transition from a logarithmic (at temperatures below 300 °C) to parabolic (between 300 – 600 °C) oxidation [73]. Such an enhancement in the oxygen uptake can embrittle it, and, in turn, lead to the deteriorated fatigue resistance.

While the FCG behavior in the Paris regime deteriorated as the temperature increased, ΔK_o appears to remain invariant with an increasing temperature (and even slightly improved), which seems counterintuitive (Table 4). Based on the oxide-induced surface discoloration that was observed after elevated temperature tests (shown in Fig. 16), it is hypothesized that this phenomenon occurs due to

the oxide-induced crack closure [55]. To probe the effect of oxide thickness on crack closure, we interrupted the high temperature FCG tests near the threshold regime and made CMOD measurements at room temperature. (While techniques to perform such measurements at high temperatures are available, they are challenging from the accuracy point of view. We assume that the oxide layer does not grow during the cooling process.) Surprisingly, as the FCG testing temperature is increased, we did not detect any closure, except at RT, as shown in Fig. 17. This crack closure at RT is roughness-induced, as shown by the serrated crack growth in Figs. 13a and e for the AP and HT samples, respectively.

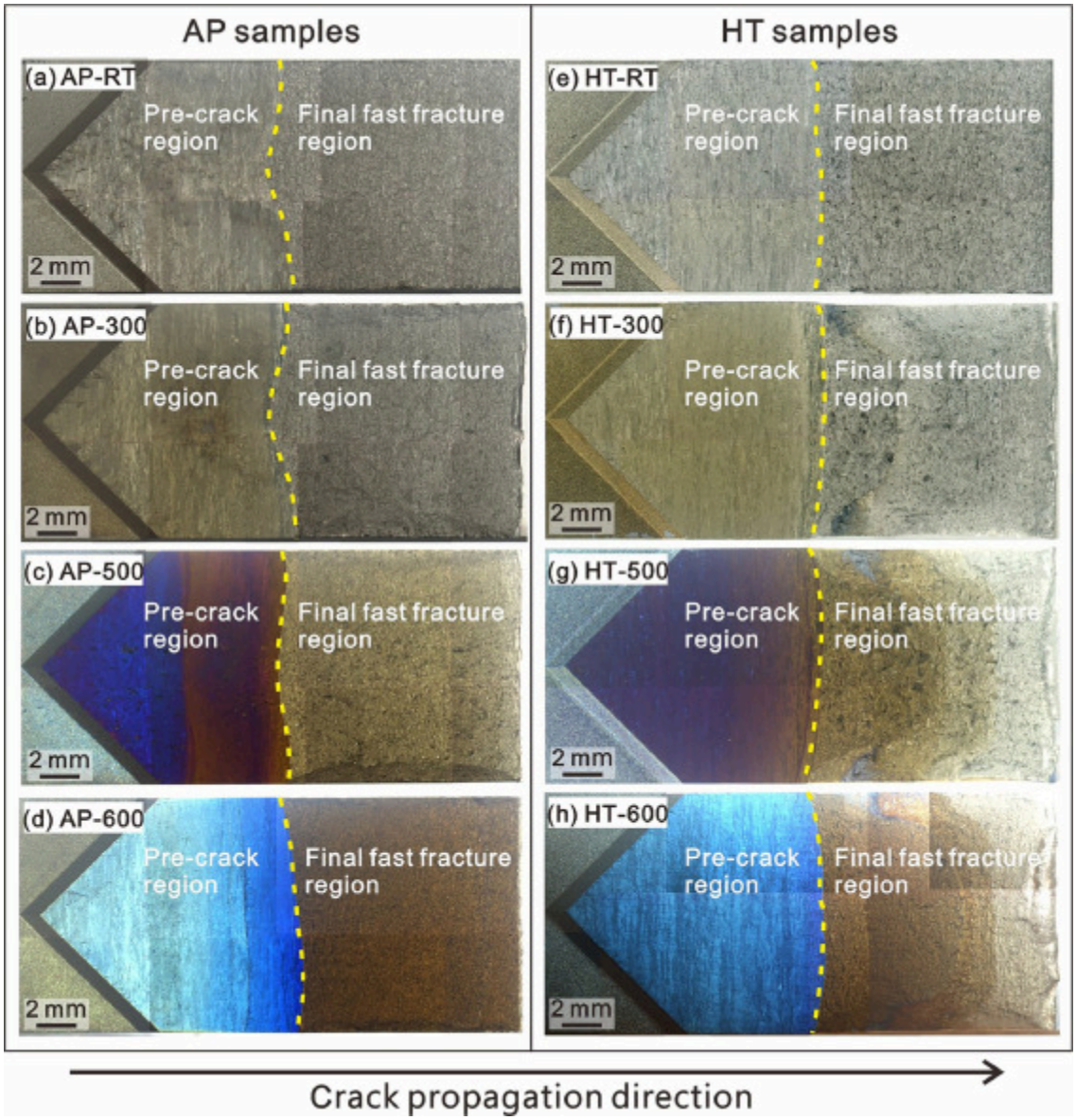

1. Download: Download high-res image (2MB)
2. Download: Download full-size image

Fig. 16. Representative fracture surface after FCG and fracture toughness test for (a-d) AP and (e-h) HT, tested at (a, e) RT, (b, f) 300 °C, (c, g) 500 °C, and (d, h) 600 °C, showing the oxide color variation under different temperature conditions.

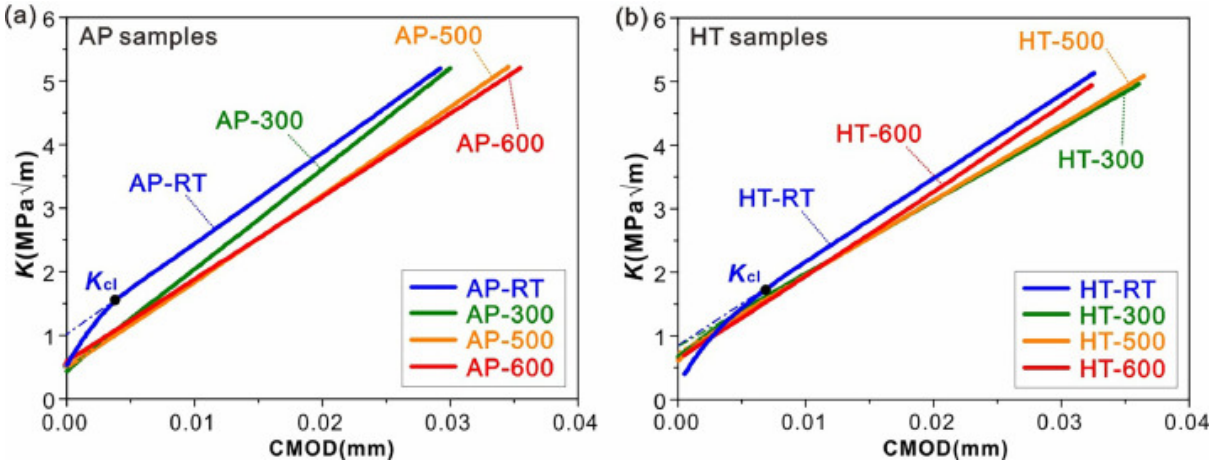

1. Download: Download high-res image (483KB)
2. Download: Download full-size image

Fig. 17. Fatigue crack closure analysis: representative stress intensity factor *K* versus CMOD curves for the (a) AP and (b) HT samples at room temperature, associated with C(T) samples with fatigue cracks grown to the near-threshold regime at different temperatures. K_{cl} is the stress intensity factor at crack closure.

We propose that specific intrinsic material behavior at high temperatures play a role in the progressive crack blunting, observed in Fig. 13, as test temperatures rise, potentially leading to an enhancement in ΔK_o. This phenomenon occurs in tandem with the gradual straightening of fatigue cracks, as illustrated again in Fig. 13. These characteristics near the fatigue crack tip near the threshold consistently suggest the formation of a significantly larger deformation zone relative to the local microstructure, especially at elevated temperatures. This naturally prompts us to consider the reduced yield strength at elevated temperatures as a potential and primary factor, which may result in a plastic zone size that is extensive enough to induce straight crack growth through multi-slip mechanisms.

To understand the crack-tip blunting in the near-threshold FCG, it is necessary to consider the cyclic plastic zone, r_c, ahead of the crack tip under plane strain conditions, which is given by [3,55]: rc=13π(ΔK02σy)2. Generally, the FCG behavior changes from being microstructure-insensitive to -sensitive when the cyclic plastic zone size, rc=13π(ΔKT2σy)2, is equivalent to the characteristic size, *l**, of the material under investigation [3,55]. In this context, the average prior β size (λ_β) and average lath width (λ_α) are both considered for *l**. Then, the transition stress intensity factor range, ΔKTβ=2σy3πλβ, and ΔKTα=2σy3πλα for the AP and HT samples tested at different temperatures are calculated and listed in Table 4, to probe the role of YS induced plastic zone size in facilitating straight crack growth. These values represent Δ*K* at which the plastic zone size is comparable to the microstructural length scale (especially the α/α' lath width). If ΔK_o were greater than ΔK_T it would signify that the plastic zone size within the sample is sufficiently large to evade crack interaction with the local microstructure at the fatigue threshold region. However, it was observed that for all specimens, ΔK_o was lower than $\Delta K_{T\alpha}$, and would typically lead to serrated FCG due to interactions with the local microstructure [3,55]. Surprisingly, this phenomenon did not occur, prompting us to consider the possibility of creep-induced crack tip blunting instead.

As opposed to plasticity-induced crack blunting at room temperature, creep-induced crack blunting takes place at high temperatures and can lead to the crack tip deformation, without needing to

overcome the local YS. As creep is involved, the blunting process is time-sensitive and can be substantial when the loading frequency (Hz) is low, or when the *da/dN* is slow, i.e., near the ΔK_o region. More importantly, with time, the blunting can become significant, even when the plastic zone size is small. In a sharp crack that experiences high temperature, the stress concentrates at the crack tip, leading to the highest creep rate within it, changing the shape of the crack tip towards a blunter form. A schematic illustrating the extent of crack blunting as a result of deformation zone size with and without creep is given in Fig. 18.

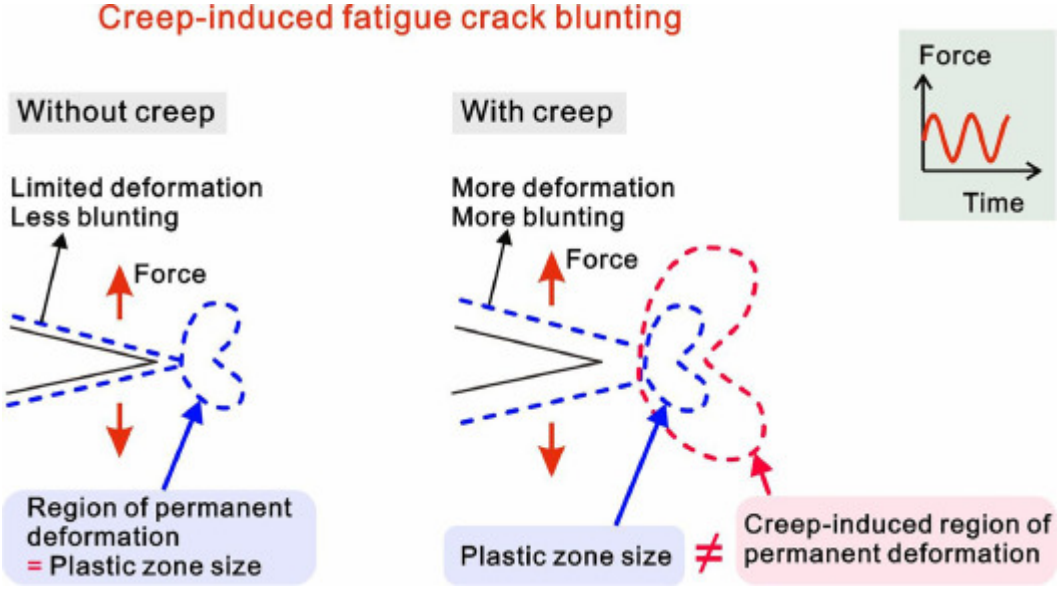

1. Download: Download high-res image (376KB)
2. Download: Download full-size image

Fig. 18. Schematic diagrams illustrating the extent of fatigue crack blunting, influenced by the size of the permanent deformation zone, both with and without creep.

Creep in titanium can occur even at room temperature [75]. Additionally, the decomposition of the α' phase in α/β alloys above 400 °C, as observed in this study as well as published literature [[47], [76]], underscores the significance of diffusion-driven creep at the temperatures examined in our study. While previous studies have linked creep-fatigue behavior to a declining FCG rate at higher ΔK values [77,78], its specific impact on ΔK_o has received limited attention. Our hypothesis, suggesting the advantageous effects of creep-induced crack blunting, gains support from prior research on Ti-1100, a near- α/β -processed alloy [74]. In that study, environmental factors were isolated by conducting tests in a vacuum environment. Tests were performed at various frequencies (0.05, 0.5, and 10 Hz) while maintaining a constant stress intensity factor ratio (R = 0.1) at 593 °C. Lower loading frequencies provide more time for creep during each cycle. At high ΔK values (around 30 MPa$\sqrt{m}$), the FCG rate increased with lower cyclic frequencies. However, as it approached ΔK_o, a more pronounced deceleration in the FCG rate was observed at lower frequencies, resulting in a crossover in the FCG curves. Similar trends were noted for Ti-6242, an α/β alloy [79,80]. It is important to note that due to the low-frequency cycling used, achieving FCG rates below 10^{-9} was challenging in these studies.

The deterioration of FCG at high ΔK values due to creep can be attributed to changes in slip length, resulting from the temperature-induced relaxation of the back stress at the colony boundaries [77]. This process eventually leads to the slip length extending to the prior β grain boundaries, creating intense dislocation pileups. However, when considering ΔK_o, the benefit of creep-fatigue induced blunting outweighs the slip length modification, leading to the pronounced deceleration of FCG rate

at low ΔK values. In contrast to our study, a prior investigation on Ti-6Al-4V, employing a significantly higher loading frequency (100 Hz) and R = 0.35, showed a decline in ΔK_o with increasing temperature, indicating the influence of temperature on ΔK_o when creep effect is less pronounced [73].

However, the creep-induced blunting explanation falls short in elucidating the ΔK_o dip observed in HT-300. This aspect is particularly intriguing considering that the presence of the β phase should have amplified the creep rate. As already mentioned, the self-diffusion rate within β phase is higher, by about two orders of magnitude, than that in α [43], facilitating dislocation climb and creep. Consequently, this should have led to blunting and an enhanced ΔK_o, especially when compared to the HT-RT and AP-300 samples. Surprisingly, our observations revealed that the crack tip in HT-300 (shown in Fig. 13f) was sharper compared to that in the AP-300 sample (shown in Fig. 13b).

The most plausible explanation for this phenomenon is hydrogen-assisted crack growth, with the β phase acting as a lower resistant pathway for hydrogen diffusion compared to the densely packed α phase [81,82]. This hypothesis is substantiated by the concurrent appearance of the double Paris exponent phenomenon, illustrated in Fig. 11b, similarly observed during the FCG studies on Ti-6Al-4V conducted under a hydrogen atmosphere [83]. The slower crack growth rate allows sufficient time for hydrogen to reach the crack tip and attain a critical concentration that embrittles the alloy. However, the specific concentration required remains undocumented in the literature. In addition, prior studies on Ti-6Al-4V with a bimodal microstructure that is similar to that of the present study have shown this phenomenon through FCG tests at 300 – 350 °C under ambient air condition [84,85]. In one of these studies, the testing of Ti-6Al-4V at 300 °C encompassed various atmospheres, including air, argon, and argon + water. These experiments highlighted that water primarily contributes to the observed double Paris exponent phenomenon at elevated temperatures. It is worth noting that when a fresh crack surface is exposed, oxide formation on the surface can release hydrogen from the dissociated water molecules [86], which are then absorbed into the crack tip region. (The measured relative humidity in the lab where the mechanical tests reported in this paper is 63±1 %. Such relatively high humidity, for a lab setting, is due to the fact that Singapore is a tropical country where relative humidity levels in excess of 80 % are common.) Note that the consideration of differences in oxygen pickup at a specific temperature due to microstructural differences is omitted, as it was shown in a prior work on Ti-6Al-4V that there are negligible differences in oxide scale and oxygen diffusion zone thickness for 500–600 °C with different microstructures (including α' martensite vs. lamellar α with β ligaments) [[33], [34], [35]].

In the case of AP-300, the absence of the β phase eliminates the faster diffusion pathway for hydrogen, hence the absence of double Paris exponent phenomenon. This is further reinforced by FCG observations at high and low ΔK values, where fewer secondary cracks are detected in AP-300 (see Fig. 12b and Fig. 13b) compared to HT-300 (see Fig. 12f and Fig. 13f). Meanwhile, at temperatures of 500 °C or higher, the influence of hydrogen embrittlement-induced crack growth is outweighed by creep-induced blunting. The quantification of such localized hydrogen increase with thermal desorption spectroscopy is challenging, as it is difficult to retain the temporary increase in hydrogen concentration near the fracture surface at high temperature, which would spread to the entire volume of the CT specimen. For future prospects, the use of miniaturized samples to perform FCG, specifically to allow for the measurement of minute increases in hydrogen content postmortem, is a sound direction to further this area of research.

In summary, the interplay between hydrogen-assisted FCG, creep-fatigue, and their connection with the presence of the β phase adds intricacy to the interesting fracture behavior of the LPBF α/β titanium

alloy at elevated temperatures.

5. Summary

The fracture behaviors of an α/β titanium alloy, manufactured using LPBF, were investigated over the temperature range of RT to 600 °C, in both the AP and HT states. The heat treatment was designed to decompose the α' martensitic lath structure prevalent in the AP state of the LPBF alloy into α laths of uniform size while introducing β ligaments. The alloy, in both the AP and HT states, exhibited a common trend of decreasing strength as the temperature increased. However, a significant divergence in terms of ductility emerges beyond 300 °C, where the AP state exhibited a substantial drop in ductility due to void nucleation and propagation along prior β boundaries, while the HT state exhibited a continuous improvement in ductility with rising temperature, attributed to the presence of β ligaments. The fracture initiation toughness peaked at 300 °C for both states (with the HT state consistently outperforming the AP state), highlighting that the trends in ductility and fracture initiation toughness do not go in tandem. Within the Paris regime of fatigue crack growth, resistance to FCG generally decreased with increasing temperatures, while ΔK_o values remained relatively invariant, exhibiting improvement in most cases. This phenomenon was primarily associated with the influence of creep-induced crack tip blunting. Notably, the HT state tested at 300 °C displayed unique characteristics, including a dip in ΔK_o with temperature and the emergence of a double Paris exponent, indicative of hydrogen-assisted fatigue crack growth – facilitated by β phase's role as a conduit for hydrogen diffusion.

CRediT authorship contribution statement

Meishen Xie: Conceptualization, Investigation, Methodology, Visualization, Writing – original draft. **Sheng Huang:** Conceptualization, Investigation, Methodology, Supervision, Visualization, Writing – original draft, Writing – review & editing. **Zhi Wang:** Conceptualization, Supervision, Funding acquisition, Project administration, Resources. **Upadrasta Ramamurty:** Funding acquisition, Project administration, Resources, Supervision, Writing – review & editing.

Declaration of competing interest

The authors declare that they have no known competing financial interests or personal relationships that could have appeared to influence the work reported in this paper.

Acknowledgments

The authors acknowledge the financial support from the Guangdong Natural Science Foundation (2023A1515011569, 2024A1515010425), and China Scholarship Council (CSC). The work at Nanyang Technological University was supported by Agency for Science, Technology and Research (A*STAR) of Singapore via the Structural Metal Alloys Programme (No. A18B1b0061).

Appendix. Supplementary materials

Download: Download Word document (6MB)

References

1. [1]

P. Kumar, U. Ramamurty

High cycle fatigue in selective laser melted Ti-6Al-4V

Acta Mater., 194 (2020), pp. 305-320, 10.1016/j.actamat.2020.05.041

View PDFView articleView in ScopusGoogle Scholar

2. [2]

P. Kumar, O. Prakash, U. Ramamurty

Micro-and meso-structures and their influence on mechanical properties of selectively laser melted

Ti-6Al-4V
Acta Mater., 154 (2018), pp. 246-260, 10.1016/j.actamat.2018.05.044
View PDFView articleView in ScopusGoogle Scholar
3. [3]
P. Kumar, U. Ramamurty
Microstructural optimization through heat treatment for enhancing the fracture toughness and fatigue crack growth resistance of selective laser melted Ti–6Al–4V alloy
Acta Mater., 169 (2019), pp. 45-59, 10.1016/j.actamat.2019.03.003
View PDFView articleGoogle Scholar
4. [4]
S. Huang, R.L. Narayan, J.H.K. Tan, S.L. Sing, W.Y. Yeong
Resolving the porosity-unmelted inclusion dilemma during in-situ alloying of Ti34Nb via laser powder bed fusion
Acta Mater., 204 (2021), Article 116522, 10.1016/j.actamat.2020.116522
View PDFView articleView in ScopusGoogle Scholar
5. [5]
C.C. Zhang, H.L. Wei, T.T. Liu, L.Y. Jiang, T. Yang, W.H. Liao
Influences of residual stress and micro-deformation on microstructures and mechanical properties for Ti-6.5Al-3.5Mo-1.5Zr-0.3Si alloy produced by laser powder bed fusion
J. Mater. Sci. Technol., 75 (2021), pp. 174-183, 10.1016/j.jmst.2020.08.061
View PDFView articleView in ScopusGoogle Scholar
6. [6]
Z. Zhu, P. Kumar, F.L. Ng, H.L. Seet, U. Ramamurty, S.M.L. Nai
Heat treatment effect on the microstructure and elevated temperature tensile property of the Ti6242S alloy fabricated via laser powder bed fusion
J. Alloys Compd., 925 (2022), Article 166656, 10.1016/j.jallcom.2022.166656
View PDFView articleView in ScopusGoogle Scholar
7. [7]
X. Wu, D. Zhang, Y. Guo, T. Zhang, Z. Liu
Microstructure and mechanical evolution behavior of LPBF (laser powder bed fusion)-fabricated TA15 alloy
J. Alloys Compd., 873 (2021), Article 159639, 10.1016/j.jallcom.2021.159639
View PDFView articleView in ScopusGoogle Scholar
8. [8]
J. Liu, Y. Li, Y. Zhu, Y. Yang, R. Zhang, Z. Zhang, A. Huang, K. Zhang
Enhancing high-temperature strength and ductility in laser powder bed fusion Ti–6.5Al–2Zr–1Mo–1V alloy via heat treatment optimization
Mater. Sci. Eng. A., 859 (2022), Article 144201, 10.1016/j.msea.2022.144201
View PDFView articleView in ScopusGoogle Scholar
9. [9]
S. Huang, S.L. Sing, W.Y. Yeong
Selective laser melting of Ti42Nb composite powder and the effect of laser re-melting
Key Eng. Mater., 801 KEM (2019), pp. 270-275, 10.4028/www.scientific.net/KEM.801.270
View in ScopusGoogle Scholar

10. [10]
S. Huang, S.L. Sing, G. de Looze, R. Wilson, W.Y. Yeong
Laser powder bed fusion of titanium-tantalum alloys: compositions and designs for biomedical applications
J. Mech. Behav. Biomed. Mater., 108 (2020), Article 103775, 10.1016/j.jmbbm.2020.103775
View PDFView articleView in ScopusGoogle Scholar
11. [11]
S. Huang, P. Kumar, W.Y. Yeong, R.L. Narayan, U. Ramamurty
Fracture behavior of laser powder bed fusion fabricated Ti41Nb via in-situ alloying
Acta Mater., 225 (2022), Article 117593, 10.1016/j.actamat.2021.117593
View PDFView articleView in ScopusGoogle Scholar
12. [12]
M.T. Hasib, H.E. Ostergaard, Q. Liu, X. Li, J.J. Kruzic
Tensile and fatigue crack growth behavior of commercially pure titanium produced by laser powder bed fusion additive manufacturing
Addit. Manuf., 45 (2021), Article 102027, 10.1016/j.addma.2021.102027
View PDFView articleView in ScopusGoogle Scholar
13. [13]
Y. Zhang, Z. Zhai, Z. Wu, W. Lin, R. Yang, Z. Zhang
Tailoring high-temperature mechanical properties of laser powder bed fusion Ti-6.5Al-2Zr-1Mo-1V alloy via microstructure design
Mater. Des., 236 (2023), Article 112488, 10.1016/j.matdes.2023.112488
View PDFView articleView in ScopusGoogle Scholar
14. [14]
T. DebRoy, H.L. Wei, J.S. Zuback, T. Mukherjee, J.W. Elmer, J.O. Milewski, A.M. Beese, A. Wilson-Heid, A. De, W. Zhang
Additive manufacturing of metallic components – Process, structure and properties
Prog. Mater. Sci., 92 (2018), pp. 112-224, 10.1016/j.pmatsci.2017.10.001
View PDFView articleView in ScopusGoogle Scholar
15. [15]
D. Herzog, V. Seyda, E. Wycisk, C. Emmelmann
Additive manufacturing of metals
Acta Mater., 117 (2016), pp. 371-392, 10.1016/j.actamat.2016.07.019
View PDFView articleView in ScopusGoogle Scholar
16. [16]
M. Laleh, E. Sadeghi, R.I. Revilla, Q. Chao, N. Haghdadi, A.E. Hughes, W. Xu, I. De Graeve, M. Qian, I. Gibson, M.Y. Tan
Heat treatment for metal additive manufacturing
Prog. Mater. Sci., 133 (2023), Article 101051, 10.1016/j.pmatsci.2022.101051
View PDFView articleView in ScopusGoogle Scholar
17. [17]
M.V. Pantawane, S. Dasari, S.A. Mantri, R. Banerjee, N.B. Dahotre
Rapid thermokinetics driven nanoscale vanadium clustering within martensite laths in laser powder bed fused additively manufactured Ti6Al4V

Mater. Res. Lett., 8 (2020), pp. 383-389, 10.1080/21663831.2020.1772396
View in ScopusGoogle Scholar
18. [18]
M.V. Pantawane, S. Sharma, A. Sharma, S. Dasari, S. Banerjee, R. Banerjee, N.B. Dahotre
Coarsening of martensite with multiple generations of twins in laser additively manufactured Ti6Al4V
Acta Mater., 213 (2021), Article 116954, 10.1016/j.actamat.2021.116954
View PDFView articleView in ScopusGoogle Scholar
19. [19]
J. Yang, H. Yu, J. Yin, M. Gao, Z. Wang, X. Zeng
Formation and control of martensite in Ti-6Al-4V alloy produced by selective laser melting
Mater. Des., 108 (2016), pp. 308-318, 10.1016/j.matdes.2016.06.117
View PDFView articleView in ScopusGoogle Scholar
20. [20]
J.J. Lewandowski, M. Seifi
Metal additive manufacturing: a review of mechanical properties
Annu. Rev. Mater. Res., 46 (2016), pp. 151-186, 10.1146/annurev-matsci-070115-032024
View in ScopusGoogle Scholar
21. [21]
P. Edwards, M. Ramulu
Effect of build direction on the fracture toughness and fatigue crack growth in selective laser melted Ti-6Al-4V
Fatigue Fract. Eng. Mater. Struct., 38 (2015), pp. 1228-1236, 10.1111/ffe.12303
View in ScopusGoogle Scholar
22. [22]
K.S. Ravichandran, A.K. Vasudevan
Fracture resistance of structural alloys
Fatigue Fract, 19 (2018), pp. 381-392, 10.31399/asm.hb.v19.a0002379
Google Scholar
23. [23]
A. Zafari, M.R. Barati, K. Xia
Controlling martensitic decomposition during selective laser melting to achieve best ductility in high strength Ti-6Al-4V
Mater. Sci. Eng. A., 744 (2019), pp. 445-455, 10.1016/j.msea.2018.12.047
View PDFView articleView in ScopusGoogle Scholar
24. [24]
Z. Zhu, F.L. Ng, H.L. Seet, S.M.L. Nai
Tailoring the microstructure and mechanical property of laser powder bed fusion fabricated Ti–6Al–2Sn–4Zr–2Mo via heat treatment
J. Alloys Compd., 895 (2022), Article 162648, 10.1016/j.jallcom.2021.162648
View PDFView articleView in ScopusGoogle Scholar
25. [25]
D. Zhang, L. Wang, H. Zhang, A. Maldar, G. Zhu, W. Chen, J.S. Park, J. Wang, X. Zeng
Effect of heat treatment on the tensile behavior of selective laser melted Ti-6Al-4V by in situ X-ray characterization

Acta Mater., 189 (2020), pp. 93-104, 10.1016/j.actamat.2020.03.003
View PDFView articleGoogle Scholar
26. [26]
C. Leyens, M. Peters, Titanium and Titanium Alloys: fundamentals and Applications, (2003). https://doi.org/10.1002/3527602119.
Google Scholar
27. [27]
J.C. Williams, R.R. Boyer
Opportunities and issues in the application of titanium alloys for aerospace components
Metals. (Basel), 10 (2020), 10.3390/met10060705
Google Scholar
28. [28]
R.R. Boyer
An overview on the use of titanium in the aerospace industry
Mater. Sci. Eng. A., 213 (1996), pp. 103-114, 10.1016/0921-5093(96)10233-1
View PDFView articleView in ScopusGoogle Scholar
29. [29]
X.Z. Ma, Z.L. Xiang, M.Z. Ma, Y.P. Cui, W.M. Ren, Z.T. Wang, J.C. Huang, Z.Y. Chen
Investigation of microstructures, textures, mechanical properties and fracture behaviors of a newly developed near α titanium alloy
Mater. Sci. Eng. A. (2020), p. 775, 10.1016/j.msea.2020.138996
Google Scholar
30. [30]
C. Fleißner-Rieger, T. Pfeifer, T. Jörg, T. Kremmer, M. Brabetz, H. Clemens, S. Mayer
Selective laser melting of a near-α Ti6242S Alloy for high-performance automotive parts
Adv. Eng. Mater., 23 (2021), Article 2001194, 10.1002/adem.202001194
View in ScopusGoogle Scholar
31. [31]
S. Chang, W. Du, Z. Zhao, P. Bai
Microstructure and high temperature-mechanical properties of TiC/Graphene/Ti6Al4V composite formed by laser powder bed fusion
Metals. (Basel) (2023), p. 13, 10.3390/met13010163
Google Scholar
32. [32]
J. Stringer
The oxidation of titanium in oxygen at high temperatures
Acta Metall, 8 (1960), pp. 758-766, 10.1016/0001-6160(60)90170-X
View PDFView articleView in ScopusGoogle Scholar
33. [33]
A. Casadebaigt, J. Hugues, D. Monceau
High temperature oxidation and embrittlement at 500–600°C of Ti-6Al-4V alloy fabricated by Laser and Electron Beam Melting
Corros. Sci. (2020), p. 175, 10.1016/j.corsci.2020.108875
Google Scholar

34. [34]
W.L. Finlay, J.A. Snyder
Effects of three interstitial solutes (nitrogen, oxygen, and carbon) on the mechanical properties of high-purity, alpha titanium
Jom, 2 (1950), pp. 277-286, 10.1007/bf03399001
Google Scholar
35. [35]
R.N. Shenoy, J. Unnam, R.K. Clark
Oxidation and embrittlement of Ti-6Al-2Sn-4Zr-2Mo alloy
Oxid. Met., 26 (1986), pp. 105-124, 10.1007/BF00664276
View in ScopusGoogle Scholar
36. [36]
Z. Zhou, Y. Liu, X. Liu, L. Wu
High-temperature tensile and creep properties of TiB-reinforced Ti6Al4V composite fabricated by laser powder bed fusion
Mater. Charact., 200 (2023), Article 112859, 10.1016/j.matchar.2023.112859
View PDFView articleView in ScopusGoogle Scholar
37. [37]
Y. He, Y. Ma, W. Zhang, Z. Wang
Anisotropic tensile and fatigue properties of laser powder bed fusion Ti6Al4V under high temperature
Eng. Fract. Mech. (2022), p. 276, 10.1016/j.engfracmech.2022.108948
View in ScopusGoogle Scholar
38. [38]
Q. Li, S. Huang, Y. Zhao, Y. Gao, U. Ramamurty
Simultaneous enhancements of strength, ductility, and toughness in a TiB reinforced titanium matrix composite
Acta Mater., 254 (2023), Article 118995, 10.1016/j.actamat.2023.118995
View PDFView articleView in ScopusGoogle Scholar
39. [39]
A. Gupta, C.J. Bennett, W. Sun, N. Neate
On the microstructural evolution and failure mechanism in laser powder bed fusioned Ti-6Al-4V during low cycle fatigue at room and elevated temperatures
J. Mater. Res. Technol., 21 (2022), pp. 4299-4319, 10.1016/j.jmrt.2022.10.141
View PDFView articleView in ScopusGoogle Scholar
40. [40]
T. Mishurova, K. Artzt, B. Rehmer, J. Haubrich, L. Ávila, F. Schoenstein, I. Serrano-Munoz, G. Requena, G. Bruno
Separation of the impact of residual stress and microstructure on the fatigue performance of LPBF Ti-6Al-4V at elevated temperature
Int. J. Fatigue. (2021), p. 148, 10.1016/j.ijfatigue.2021.106239
Google Scholar
41. [41]
L.M. Viespoli, S. Bressan, T. Itoh, N. Hiyoshi, K.G. Prashanth, F. Berto
Creep and high temperature fatigue performance of as build selective laser melted Ti-based 6Al-4V

titanium alloy
Eng. Fail. Anal., 111 (2020), Article 104477, 10.1016/j.engfailanal.2020.104477
View PDFView articleView in ScopusGoogle Scholar
42. [42]
S. Spigarelli, C. Paoletti, M. Cabibbo, E. Cerri, E. Santecchia
On the creep performance of the Ti-6Al-4V alloy processed by additive manufacturing
Addit. Manuf. (2022), p. 49, 10.1016/j.addma.2021.102520
Google Scholar
43. [43]
D. Dye, Ti Alloy Mechanics II; Other Ti alloys, Lect. Notes MSE307 Eng. Alloy. 2014-15 L8. (2015).
Google Scholar
44. [44]
ASTM E8/E8M-22
Standard test methods for tension testing of metallic materials
ASTM Int, West Conshohocken, PA (2022)
Google Scholar
45. [45]
ASTM E399-23
Standard test method for plane-strain fracture toughness of metallic materials
ASTM Int., West Conshohocken, PA (2023)
Google Scholar
46. [46]
ASTM E647−23a
Standard test method for measurement of fatigue crack growth rates
ASTM Int., West Conshohocken, PA (2023)
Google Scholar
47. [47]
W. Xu, M. Brandt, S. Sun, J. Elambasseril, Q. Liu, K. Latham, K. Xia, M. Qian
Additive manufacturing of strong and ductile Ti-6Al-4V by selective laser melting via in situ martensite decomposition
Acta Mater., 85 (2015), pp. 74-84, 10.1016/j.actamat.2014.11.028
View PDFView articleView in ScopusGoogle Scholar
48. [48]
B. Vrancken, L. Thijs, J.P. Kruth, J. Van Humbeeck
Microstructure and mechanical properties of a novel β titanium metallic composite by selective laser melting
Acta Mater., 68 (2014), pp. 150-158, 10.1016/j.actamat.2014.01.018
View PDFView articleView in ScopusGoogle Scholar
49. [49]
W. Xu, E.W. Lui, A. Pateras, M. Qian, M. Brandt
In situ tailoring microstructure in additively manufactured Ti-6Al-4V for superior mechanical performance
Acta Mater., 125 (2017), pp. 390-400, 10.1016/j.actamat.2016.12.027
View PDFView articleView in ScopusGoogle Scholar

50. [50]
E. Alabort, Y.T. Tang, D. Barba, R.C. Reed
Alloys-by-design: a low-modulus titanium alloy for additively manufactured biomedical implants
Acta Mater., 229 (2022), 10.1016/j.actamat.2022.117749
Google Scholar
51. [51]
P.A. Kobryn, S.L. Semiatin
The laser additive manufacture of Ti-6Al-4V
Jom, 53 (2001), pp. 40-42, 10.1007/s11837-001-0068-x
View in ScopusGoogle Scholar
52. [52]
G.J. Marshall, W.J. Young, S.M. Thompson, N. Shamsaei, S.R. Daniewicz, S. Shao
Understanding the microstructure formation of Ti-6Al-4V during direct laser deposition via in-situ thermal monitoring
Jom, 68 (2016), pp. 778-790, 10.1007/s11837-015-1767-z
View in ScopusGoogle Scholar
53. [53]
G.M. Ter Haar, T.H. Becker
Selective laser melting produced Ti-6Al-4V: post-process heat treatments to achieve superior tensile properties
Materials. (Basel), 11 (2018), 10.3390/ma11010146
Google Scholar
54. [54]
C. Leyens, M. Peters, Titanium and Titanium Alloys: fundamentals and Applications, 2003.
Google Scholar
55. [55]
S. Suresh, Fatigue of materials (2nd ed.), 2012. https://doi.org/10.1017/CBO9780511806575.
Google Scholar
56. [56]
M.E. Kassner, T.A. Hayes
Creep cavitation in metals
Int. J. Plast., 19 (2003), pp. 1715-1748, 10.1016/S0749-6419(02)00111-0
View PDFView articleView in ScopusGoogle Scholar
57. [57]
F.J. Seco, A.M. Irisarri
Creep failure mechanisms of a Ti-6Al-4V thick plate
Fatigue Fract. Eng. Mater. Struct., 24 (2001), pp. 741-750, 10.1046/j.1460-2695.2001.00426.x
View in ScopusGoogle Scholar
58. [58]
V.M.C.A. De Oliveira, M.C.L. Da Silva, C.G. Pinto, P.A. Suzuki, J.P.B. Machado, V.M. Chad, M.J.R. Barboza
Short-term creep properties of Ti-6Al-4V alloy subjected to surface plasma carburizing process
J. Mater. Res. Technol., 4 (2015), pp. 359-366, 10.1016/j.jmrt.2015.05.006
View PDFView articleView in ScopusGoogle Scholar

59. [59]
A. Lange, J. Lindemann, A. Styczynski, L. Wagner
Optical and scanning electron microscopic investigations of creep damage in the high temperature titanium alloy TIMETAL 1100
Pract. Metallogr., 35 (1998), pp. 469-479, 10.1515/pm-1998-350904
View in ScopusGoogle Scholar
60. [60]
N.E. Paton, M.W. Mahoney
Creep of titanium-silicon alloys
Metall. Trans. A., 7 (1976), pp. 1685-1694, 10.1007/BF02817886
View in ScopusGoogle Scholar
61. [61]
T.L. Sham, A. Needleman
Effects of triaxial stressing on creep cavitation of grain boundaries
Acta Metall, 31 (1983), pp. 919-926, 10.1016/0001-6160(83)90120-7
View PDFView articleView in ScopusGoogle Scholar
62. [62]
Y. Murakami
Stress Intensity Factors Handbook, 3 (1993), p. 1063, 10.1115/1.2900983
J. Appl. Mech. 60
Google Scholar
63. [63]
K.Y. Lam, S.P. Phua
Multiple crack interaction and its effect on stress intensity factor
Eng. Fract. Mech., 40 (1991), pp. 585-592, 10.1016/0013-7944(91)90152-Q
View PDFView articleView in ScopusGoogle Scholar
64. [64]
Z. Shi, Chapter 5 - Crack Interaction and Localization, 2009. https://doi.org/10.1016/b978-0-7506-8446-0.00005-x.
Google Scholar
65. [65]
I. Sen, U. Ramamurty
Elastic modulus of Ti-6Al-4V-xB alloys with B up to 0.55 wt.%
Scr. Mater., 62 (2010), pp. 37-40, 10.1016/j.scriptamat.2009.09.022
View PDFView articleView in ScopusGoogle Scholar
66. [66]
Z. Liu, J. Zhang, B. He, Y. Zou
High-speed nanoindentation mapping of a near-alpha titanium alloy made by additive manufacturing
J. Mater. Res., 36 (2021), pp. 2223-2234, 10.1557/s43578-021-00204-7
View in ScopusGoogle Scholar
67. [67]
J. Kang, H.S. Oh, S. Wei, G. Zhu, I. Nakahata, C.C. Tasan
An in situ study of microstructural strain localization and damage evolution in an (α+β) Ti-Al-V-Fe-Si-O alloy

Acta Mater., 242 (2023), Article 118424, 10.1016/j.actamat.2022.118424
View PDFView articleView in ScopusGoogle Scholar
68. [68]
Q. Wang, M. Wang, S. Guo, S. Tao, J. Zhou, Z. Qin, X. Lin, W. Huang
In situ tensile test of selective laser melted Ti-6.5Al-2Zr-1Mo-1V alloy at different stages of martensite decomposition
J. Mater. Sci., 58 (2023), pp. 1798-1812, 10.1007/s10853-022-08099-3
View in ScopusGoogle Scholar
69. [69]
J. Liu, K. Zhang, X. Gao, H. Wang, S. Wu, Y. Yang, Y. Zhu, A. Huang
Effects of the morphology of grain boundary α-phase on the anisotropic deformation behaviors of additive manufactured Ti–6Al–4V
Mater. Des., 223 (2022), Article 111150, 10.1016/j.matdes.2022.111150
View PDFView articleView in ScopusGoogle Scholar
70. [70]
G. Lütjering, J. Albrecht, C. Sauer, T. Krull
The influence of soft, precipitate-free zones at grain boundaries in Ti and Al alloys on their fatigue and fracture behavior
Mater. Sci. Eng. A., 468–470 (2007), pp. 201-209, 10.1016/j.msea.2006.07.168
View PDFView articleView in ScopusGoogle Scholar
71. [71]
C.M. Liu, H.M. Wang, X.J. Tian, D. Liu
Development of a pre-heat treatment for obtaining discontinuous grain boundary α in laser melting deposited Ti-5Al-5Mo-5V-1Cr-1Fe alloy
Mater. Sci. Eng. A., 604 (2014), pp. 176-182, 10.1016/j.msea.2014.03.028
View PDFView articleGoogle Scholar
72. [72]
Y. Zhang, D. Li, X. Li, X. Liu, S. Zhao, Y. Li
Creep deformation and strength evolution mechanisms of a Ti-6Al-4V alloy during stress relaxation at elevated temperatures from elastic to plastic loading
J. Mater. Sci. Technol., 126 (2022), pp. 93-105, 10.1016/j.jmst.2022.02.042
View PDFView articleGoogle Scholar
73. [73]
J.J. Burke, V. Weiss
Fatigue: environment and temperature effects
Springer, New York, NY (2013), p. 27, 10.1007/978-1-4899-1736-2
Google Scholar
74. [74]
R. Foerch, A. Madsen, H. Ghonem
Environmental interactions in high-temperature fatigue crack growth of Ti-1100
Metall. Trans. A., 24 (1993), pp. 1321-1332, 10.1007/BF02668200
View in ScopusGoogle Scholar
75. [75]
R. Dutton

A review of the low-temperature creep behaviour of Titanium
Whiteshell Lab. Pinawa, Manitoba. (1996)
Google Scholar
76. [76]
F. An, L. Zhang, C.H. Lee
Influences of grain orientation on high-cycle fatigue performance of laser powder bed fused Ti-6.5 Al-3.5 Mo-1.5 Zr-0.3 Si alloy at room temperature and 500° C
Mater. Sci. Eng. A. (2024), p. 146988, 10.1016/j.msea.2024.146988
View PDFView articleView in ScopusGoogle Scholar
77. [77]
H. Ghonem
Microstructure and fatigue crack growth mechanisms in high temperature titanium alloys
Int. J. Fatigue., 32 (2010), pp. 1448-1460, 10.1016/j.ijfatigue.2010.02.001
View PDFView articleView in ScopusGoogle Scholar
78. [78]
H. Ghonem, R. Foerch
Frequency effects on fatigue crack growth behavior in a near-α titanium alloy
Mater. Sci. Eng. A., 138 (1991), pp. 69-81, 10.1016/0921-5093(91)90677-F
View PDFView articleView in ScopusGoogle Scholar
79. [79]
F. Sansoz, H. Ghonem
Effects of loading frequency on fatigue crack growth mechanisms in α/β Ti microstructure with large colony size
Mater. Sci. Eng. A., 356 (2003), pp. 81-92, 10.1016/S0921-5093(03)00112-6
View PDFView articleView in ScopusGoogle Scholar
80. [80]
F. Sansoz, H. Ghonem
Fatigue crack growth mechanisms in Ti6242 lamellar microstructures: influence of loading frequency and temperature
Metall. Mater. Trans. A., 34 (2003), pp. 2565-2577, 10.1007/s11661-003-0016-1
View in ScopusGoogle Scholar
81. [81]
J. Kim, E. Plancher, C.C. Tasan
Hydrogenation-induced lattice expansion and its effects on hydrogen diffusion and damage in Ti–6Al–4V
Acta Mater., 188 (2020), pp. 686-696, 10.1016/j.actamat.2020.02.029
View PDFView articleView in ScopusGoogle Scholar
82. [82]
J. Kim, C.C. Tasan
Microstructural and micro-mechanical characterization during hydrogen charging: an in situ scanning electron microscopy study
Int. J. Hydrogen Energy., 44 (2019), pp. 6333-6343, 10.1016/j.ijhydene.2018.10.128
View PDFView articleView in ScopusGoogle Scholar
83. [83]

P.S. Pao, C.R. Feng, S.J. Gill
Hydrogen-assisted fatigue crack growth in beta-annealed Ti-6Al-4V
Scr. Mater., 40 (1998), pp. 19-26, 10.1016/S1359-6462(98)00395-9
View PDFView articleView in ScopusGoogle Scholar

84. [84]
J. Ding, R. Hall, J. Byrne
Effects of stress ratio and temperature on fatigue crack growth in a Ti-6Al-4V alloy
Int. J. Fatigue., 27 (2005), pp. 1551-1558, 10.1016/j.ijfatigue.2005.06.007
View PDFView articleView in ScopusGoogle Scholar

85. [85]
R.S. Piascik, R.P. Gangloff, A. Saxena, Elevated temperature effects on fatigue and fracture, 1997. https://doi.org/10.1520/STP1297-EB.
Google Scholar

86. [86]
F.E. Littman, F.M. Church
Reactions of titanium with water and aqueous solutions
Stanford Res. Inst. (1958), 10.2172/4308537
Google Scholar